Petroleum Science 20 (2023) 2009–2025

Contents lists available at ScienceDirect

Petroleum Science

journal homepage: www.keaipublishing.com/en/journals/petroleum-science

Original Paper

Ultra-deep carbonate basement reservoirs formed by polyphase fracture-related karstification in the Offshore Bohai Bay Basin, China

Jian Luo [a, b], Hai-Yang Cao [a, b, *], Domenico Chiarella [c], Ru-Lin Miao [a], Tao Ye [a, b, d], Yun-Long Xu [a, e], An-Qing Chen [a, b], Xiao-Ping Luo [a]

[a] State Key Laboratory of Oil & Gas Reservoir Geology and Exploration (Chengdu University of Technology), Chengdu, Sichuan, 610059, China
[b] Key Laboratory of Deep-time Geography and Environment Reconstruction and Applications, MNR & Institute of Sedimentary Geology, Chengdu University of Technology, Chengdu, Sichuan, 610059, China
[c] Department of Earth Sciences, Royal Holloway University of London, Surrey, TW200EX, United Kingdom
[d] Tianjin Branch of China National Offshore Oil Company Ltd., Tianjin, 300452, China
[e] Exploration and Development Research Institute, Zhongyuan Oilfield Company, SINOPEC, Puyang, Henan, 457001, China

ARTICLE INFO

Article history:
Received 13 July 2022
Received in revised form
10 November 2022
Accepted 22 March 2023
Available online 26 March 2023

Edited by Jie Hao and Teng Zhu

Keywords:
Carbonate basement reservoirs
Buried hill
Diagenetic fluid
Fracture system
Karstification
Bohai bay basin

ABSTRACT

The Palaeozoic carbonate basement of the Offshore Bohai Bay Basin (OBBB) presents considerable potential for hydrocarbon exploration. However, the multistage tectonism and complex superimposed palaeo-karstification in the area are unclear, which leads to a lack of understanding on the formation mechanism and distribution of the deep carbonate basement reservoirs. In this study, the occurrence of a fracture-vug network and its fillings in carbonate reservoirs were investigated based on borehole cores, thin sections, and image logs from the southwestern slope of the OBBB's Bozhong Sag. Then the diagenetic fluid properties of the carbonate matrix and fillings were analysed via the data of carbon, oxygen, and strontium isotopes, and major, rare elements from coring intervals. The results revealed that fracture-related karst reservoirs have lithologic selectivity inclined toward dolomite strata. The intersecting relationships, widths, and strikes of the fractures and the regional tectonic background indicate three structural fracture families: NW-, NNE-, and NNW- trending, related to the Indosinian, middle Yanshanian, and late Yanshanian orogeny, respectively. The Indosinian NW- and end-Mesozoic NNE-trending fractures produced by compressional tectonic stress mainly contributed to the formation of the basement reservoirs. The geochemistry of the calcite veins filling these fractures suggests two main types of diagenetic fluids. The fluid of autogenic recharge related to the earlier fills is karstification diffuse flow dominated by internal runoff from rainfall in the highland setting of the Indosinian thrusting orogenic belt. The other fluid of allogenic recharge related to the later fills is the main lateral freshwater flow dominated by external runoff from the catchment in the setting of the horst-lowland within the rifting basin, induced by the Yanshanian destruction of the North China Craton. Finally, the relationship between the three fracture families and two kinds of related fluids is revealed. This allows us to propose a model to understand the polyphase-superimposed fracture-related karst reservoir complexes within the deep carbonate basement of tilting fault blocks that neighbour the Bozhong hydrocarbon kitchen and predict the formation of potential plays with high accuracy.

1. Introduction

The buried hill refers to bedrock protrusions located at the base of the basin and unconformity covered by upper basinal strata (Weeks, 1967), in which the oil and gas plays are commonly referred to as basement reservoirs, an unconventional kind of Oil and gas exploration target (Lima et al., 2020; Liu et al., 2021; Wang et al., 2021). A significant exploration breakthrough was made in the BZ19-6 metagranite basement reservoir in 2019, with proven geological reserves of nearly 3×10^8 t (Hou et al., 2019), resulting in increased exploration of basement reservoirs in the Offshore Bohai Bay Basin (OBBB), North China Block. The discovery of the BZ21-22 and CFD2-1 basement traps surrounding the southwestern slope of

* Corresponding author. State Key Laboratory of Oil & Gas Reservoir Geology and Exploration (Chengdu University of Technology), Chengdu, Sichuan, 610059, China.
E-mail address: caohaiyang@cdut.edu.cn (H.-Y. Cao).

https://doi.org/10.1016/j.petsci.2023.03.021

the Bozhong Sag (Ren et al., 2018; Zhang et al., 2021) means that the deeply buried lower Palaeozoic carbonate reservoir may have major potential for future exploration (Hou et al., 2019; Ye et al., 2020a,b).

The unconformity at the top of the lower Palaeozoic carbonate, which is through the whole North China Block, is a crucial factor for forming the reservoirs. The Ordos Basin, located in its western part and maintained as an intracratonic sag basin, occurs in several plays with around a hundred meters of carbonate karst reservoir in thickness, such as Jinbian gas field. These reservoirs played at the top of Majiagou formation in the lower Palaeozoic, controlled by the multicycle penecontemporaneous karstification and Caledonian karstification under the influence of sea-level fluctuations and regional tectonic uplift (Chen et al., 2018; Xiong et al., 2019, 2022). However, the lower Palaeozoic carbonate rocks of Bohai Bay Basin located in the eastern North China Block have experienced complex tectonism (Cao et al., 2015; Jing, 2016). Different from Ordos Basin, in addition to the penecontemporaneous karstification, multiphase telogenetic karstifications also seem to play a significant role in the formation of the reservoir in Bohai Bay Basin, which is controlled by multi-phase tectonic movements. Such as the Qianmiqiao oilfield in the Huanghua Sag (a case of karstification and hydrothermal dissolution on reservoir formation) (Ma et al., 2009), and Zhuangxi oilfield in the Jiyang Sag (a case of fracture-related, and bedding-layered karstifications on reservoir formation) (Ying et al., 2005; Liu et al., 2007, 2021). Whereas, the complex relationship among multi-stage karstification, lithofacies, and fractures still lacks of an insightful understanding, especially for the OBBB' s carbonate reservoirs. This new case of the southwestern slope of the Bozhong Sag, with 11 boreholes that disclosed logging data and coring rocks of the carbonate basement, allowed us to establish a polyphase-superimposed fracture-related carbonate karstification reservoir model to provide insight into the formation of potential reservoirs, including the upper weathering epikarst and interior bedding-layered hydraulic karst.

In this paper, we present a reservoir formation model to enrich the understanding of the formation mechanism of the ultra-deep carbonate reservoirs, and provide a reference for subsequent research and exploration of deep carbonate reservoirs in the Bohai Bay Basin and other parts of the world.

2. Geological background

The Bohai Bay Basin includes the Offshore Bohai Bay Basin (OBBB) in eastern China and its coastal areas (Fig. 1a). It is tectonically located in the eastern part of the North China platform and is the most important oil and gas origin in eastern China. The study area is located on the southwestern slope of the Bozhong Sag in OBBB (Fig. 1a). The tectonic evolution of the Bohai Bay Basin is closely related to the North China Platform, with the lower Palaeozoic experiencing several tectonic phases during the Indosinian, Yanshanian, and Himalayan periods (Hou et al., 2001; Hao et al., 2014) creating the conditions for the development of polyphase karstification and fractures. The "buried hills" in the Bohai Bay Basin are mainly pre-Cenozoic strata, including Mesozoic, Palaeozoic, and Archaean deposits. The Archaean comprises metagranitoids, whereas the Palaeozoic comprises interbedded marine carbonates and continental clastic rocks forming a strata mixing (Chiarella et al., 2017). Mesozoic deposits consist of interbedded volcanic and clastic rocks. Subsurface information (i.e., borehole data) indicates that in the OBBB, the lower Palaeozoic units are widely distributed northwest of the Shaleitian and the Chengbei uplifts and on the southwestern slope of the Bozhong Sag and the Shijiutuo uplift. Owing to the differences in the lithology, the effect of tectonic movement, and the degree of denudation, the thickness of the strata, as well as the relationship among different stratigraphic units vary significantly in different regions. In the southwestern slope of the Bozhong Sag, the lower Palaeozoic is locally unconformity overlain by the Mesozoic due to the partial denudation produced by tectonic movement. Where the late Mesozoic was entirely denuded, the lower Palaeozoic is unconformably overlain by the Cenozoic (Fig. 1b). According to the regional lithological assemblage characteristics and stratigraphic sequence in the North China platform, the Bohai Bay Basin is combined with the study area's lithology, palaeontology, and geophysics. In the southwestern slope of the Bozhong Sag, the Cambrian and Ordovician comprise different units (Fig. 1c) related to depositional environments referred to tidal flats, protected platforms, and open circulation in the background of the peritidal carbonate platform (Huang et al., 2000).

3. Materials and methods

The data analysis presented in this study is based on examining samples from six drilling wells on the southwestern slope of the Bozhong Sag (BZ28-1-6D, BZ28-1-7, BZ28-1-8D, BZ21-2-A, BZ22-1-A, and CFD2-1-2). The data included cores and sidewall cores, three-dimensional seismic data, conventional and image logs and geochemical analysis of the reservoirs (Table S1).

First, we carried out detailed core observations, focused on the fracture-cutting relationship and filling characteristics shown in the core, and determined the sequence of fracture development. The density, strike, and dip of fractures in the reservoirs were determined by analyzing image logs from each well. The in-situ maximum principal stress was determined by the analysis of image logging. The evolution process of buried hills was reconstructed according to the geological profiles revealed by seismic data and combined with the regional tectonic setting. Core samples were collected according to strata (Table S1). The samples included the carbonate matrix of the reservoirs and calcite veins filled in the fractures, and the veins covered the fractures of different periods.

Magnifying glass, dilute hydrochloric acid, and magneson reagent ((4)-4-nitrophenyl azoresorcinol) were used to determine the lithology of the hand specimens. More than 400 thin sections of Palaeozoic carbonate reservoirs at different depths were prepared. The macroscopic and microscopic characteristics of the samples were determined by hand specimen observation and microscopic identification. Specific samples were then selected for different geochemical analyses. The analytical methods used in this study include major and trace elements, rare earth elements and stable isotopes (Table S1).

The sedimentary and diagenetic processes of carbonate minerals are usually accompanied by the migration of elements. Therefore, the diagenetic evolution process and fluid properties can be further clarified by the characteristics of major and trace elements of different types of minerals (Ionov and Harmer, 2002). The variability and normalized patterns of rare earth elements are influenced by multiple factors, such as diagenesis and fluid type, making it an essential tool for studying the origin of diagenetic fluids (Azmy et al., 2013; Wang et al., 2014).

We conducted the in-situ LA-ICP-MS analyse for major, trace and rare earth elements in the calcite veins filled in the fractures and their host rocks (carbonate matrix). These analyses were finished at the Wuhan SampleSolution Analytical Technology Co., Ltd., Wuhan, China. Detailed operating conditions for the laser ablation system and the ICP-MS instrument and data reduction are the same as the description by Zong et al. (2017). Laser sampling was performed using a GeolasPro laser ablation system that consists of a COMPexPro 102 ArF excimer laser (wavelength of 193 nm and maximum energy of 200 mJ) and a MicroLas optical system. An

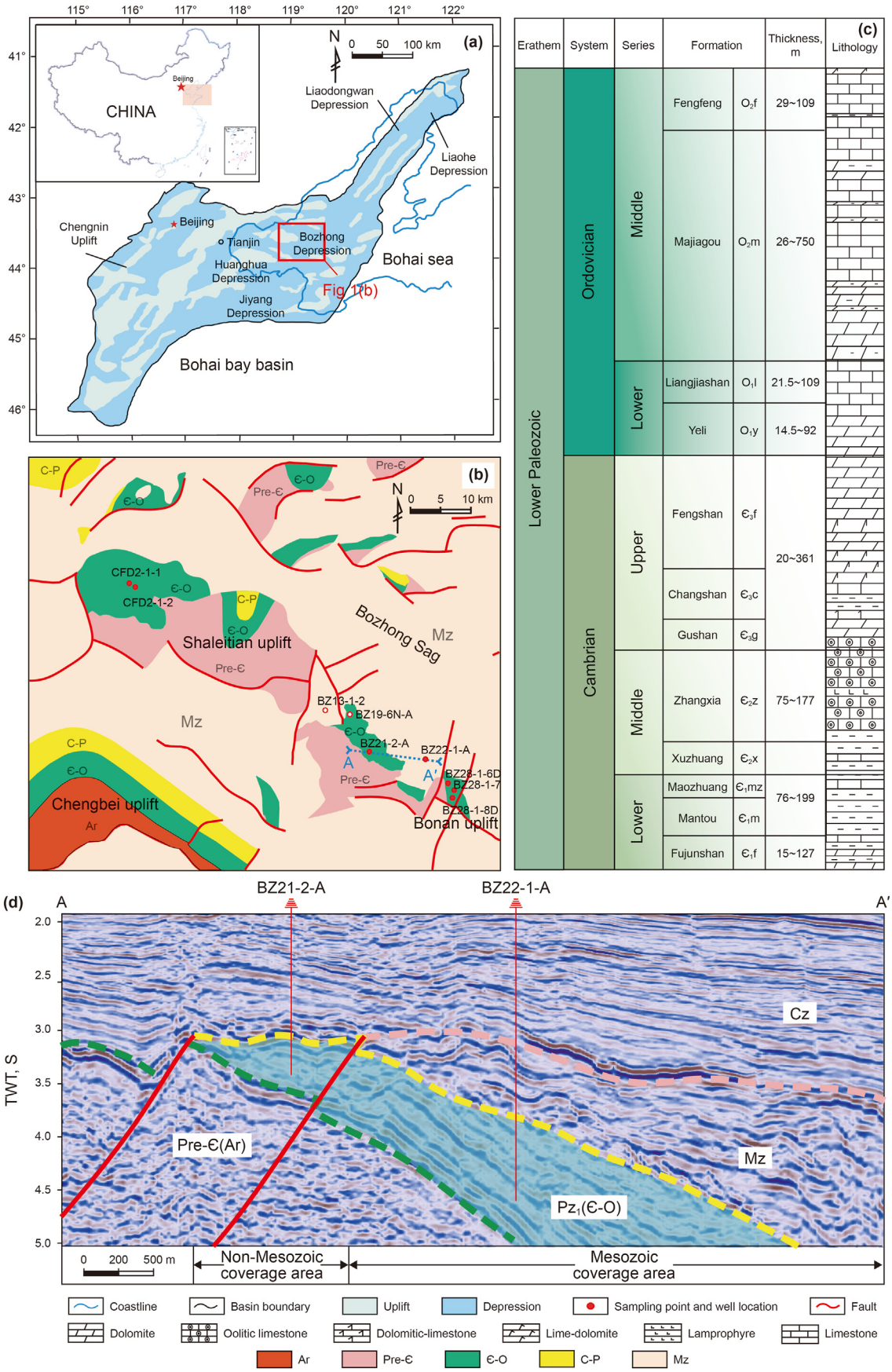

Fig. 1. (a) The location of the Bohai Bay Basin. (b) Pre-Cenozoic palaeo-geological map of the southwestern Bozhong Sag. (c) Generalised stratigraphic column of the lower Palaeozoic in the study area. (d) Interpreted seismic profile across the southwestern slope of the Bozhong Sag, and the location of the seismic profile is shown in Fig. 1b.

Agilent 7700e ICP-MS instrument was used to acquire ion-signal intensities. Helium was applied as a carrier gas. Argon was used as the make-up gas and mixed with the carrier gas via a T-connector before entering the ICP. A "wire" signal smoothing device is included in this laser ablation system (Hu et al., 2015). The spot size and frequency of the laser were set to 44 μm and 5 Hz, respectively, in this study. Trace element compositions of minerals were calibrated against various reference materials (BHVO-2G, BCR-2G and BIR-1G) (Liu et al., 2008). Each analysis incorporated a background acquisition of approximately 20–30 s followed by 50 s of data acquisition from the sample. The elements analysed include Na, Mn, Fe, Sr, and REE. An Excel-based software ICPMSDataCal was used to perform off-line selection and integration of background and analysed signals, time-drift correction and quantitative calibration for trace element analysis (Liu et al., 2008). The REE values were normalized to the REE compositions in surface Pacific water (SN) (Kawabe et al., 1998). Ce anomalies $(Ce/Ce^*)_{SN} = 2Ce_{SN}/(La_{SN} + Pr_{SN})$ and Eu anomalies $(Eu/Eu^*)_{SN} = 2Eu_{SN}/(Sm_{SN} + Gd_{SN})$ were calculated using the equations of Bau and Dulski (1996).

As an essential tracer, stable isotopes are often used to study the re-establishment of the palaeo-environment, the properties of diagenetic fluids and the migration of hydrocarbons (Shao and Ye, 1999; Cao et al., 2005; Huang et al., 2017). The carbon and oxygen isotopes of 37 samples were determined at the State Key Laboratory of Oil & Gas Reservoir Geology and Exploration (Chengdu University of Technology). The same analysis was performed on the calcite veins filling the fractures developed in the same batch of samples to reveal the properties of the reservoir dolomitisation fluid and calcite fluid filling the fractures. First, hand specimens were washed with distilled water. The sampling points of the matrix were selected from the fresh side of the rock to avoid contamination. Veins were sampled for drilling using a handheld microdrill to obtain fine powder samples. The powder samples were then dried in an oven (at 105 °C) for 2 h before being placed in a dryer for standby. A phosphoric acid solution of 100% concentration was prepared and mixed with the powder samples in a constant temperature (25 °C) water bath for 36 h to collect and purify CO_2. Then, CO_2 was analysed for C and O isotopes using a MAT251 mass spectrometer with an analysis error of less than 0.02‰ according to the VPDB standard. The specific methods can be refered to the description of McCrea (1950). The errors in the carbon and oxygen isotope analyses were less than 0.02‰.

Strontium isotope testing of the 37 × 2 powder samples was conducted at the State Key Laboratory of Oil and Gas Reservoir Geology and Exploitation (Chengdu University of Technology). 1.0 mol/L hydrochloric acid was used to dissolve the powdered samples for 2 h. After centrifugation, the supernatant was collected and separated using an AG50W-X8 cation-exchange column. Pure Sr was separated from the supernatant by elution with hydrochloric acid. Subsequently, $^{87}Sr/^{86}Sr$ values were determined using a Triton Plus thermal ionisation isotope mass spectrometer. Repeated analyses of the NBS987 standard yielded an average $^{87}Sr/^{86}Sr$ ratio of 0.71027807 ± 0.00001218 (2σ) during the analytical window.

4. Results

4.1. Petrography characterisation

The lithology of the reservoirs in the study area was mainly crystalline dolomite and limestone, with a small amount of granular dolomite and limestone (Fig. 2). Crystalline dolomite is distributed in thick layers and represents the most developed reservoirs. The crystal sizes mainly include microlite (Fig. 2a), fine crystalline (Fig. 2b), and anisocrystalline. The crystal forms are idiomorphic, semi-idiomorphic, and allomorphic. The granular material was mostly lumpy and composed of dark micritic dolomite cemented by sparry calcite (Fig. 2c). The crystalline limestones occur in a middle-thick lamellar form and are mainly distributed at the bottom of the middle Cambrian and Lower Majiagou and Yeli formations of the Ordovician (Fig. 2d). The granular limestones are mainly oolitic limestones of the Cambrian Zhangxia Formation and wormkalk limestones of the Gushan Formation, which are relatively tight (Fig. 2e).

The main reservoir space of the Lower Palaeozoic carbonate reservoirs in the study area includes dissolution pores, fractures, karst caves, and dissolution fractures. The fracture network system, composed of structural fractures and karst pores, is the most essential reservoir space. Dissolution and expansion along the fractures are also observed in the cores and thin sections (Fig. 2g and h). The Lower Palaeozoic carbonate strata in the study area experienced complex processes and diagenesis environments, and the representations of epigenetic karst under the action of atmospheric water are apparent. The appearance of unconformities, karst breccia, and expansion along the fractures and other phenomena, as well as drilling breaks and lost circulation, are often specific manifestations of epigenetic karst (Jin et al., 2014). The Lower Majiagou formation on the top of the Ordovician in the study area was unconformably in contact with the overlying Cenozoic strata, with many karst breccias observed near the unconformity (Figs. 2i and 3). Karst breccias appeared as regular or irregular bright spots in imaging logs, with the same colour as the surrounding rock and higher natural gamma ray (GR) values (Fig. 3b). Karst zones in the study area contain many dissolution pores and are partly filled with mud, resulting in high GR values of approximately 50–150 API (Fig. 3a). Additionally, mud leaks occurred during the drilling of well BZ22-1-A at the top of the Ordovician, with a loss of 117 m^3, which may be caused by fractures and caves in the karst weathering crust. In addition to the extensive range of karst developed near the weathering crust, bedding layer karst also developed in the interior of the buried hill, which manifests in the dissolution holes along the layer and regular horizontal distribution of dark spots and stratified dark lines in imaging logs (Fig. 3b).

4.2. Fracture characterisation

Macroscopic fracture characteristics. The recognised fractures mainly consist of tectonic, dissolution, and diagenetic fractures. Tectonic fractures are dominant and have the most significant influence on reservoir quality. Three families of tectonic fractures were identified using the cutting relationship of fractures in cores, sidewall cores, and thin sections (Fig. 4). The first and third families are shear fractures under compressive stress, and the second group are the fractures under tensile stress.

The first family of fractures are filled with fine crystalline calcite. The second family of fractures are partially filled with fine crystalline calcite, the proportion of filling is relatively low, and many unfilled fractures are observed in the cores. This kind of tensional fracture has a rough section and short length. The third family of fractures cut the others, indicating that they occurred later than the first two families. These fractures are filled with irregular micritic calcites mixed with argillaceous, significantly different from the filling in the first family. These two families of shearing fractures have small widths, about 0.1–1.0 cm, straight and extended farther.

Fractures response in image logs. Under image logging, tectonic, dissolution, and induced fractures exhibit various properties (Ameen et al., 2010; Awdal et al., 2016; Ye et al., 2022). In the present study, tectonic fractures are smooth and sinusoidal (Fig. 5a and b). The dissolution fracture's image logging response is primarily characterized by its rough surface, expanded pores, and even beaded pores along with the fracture (Fig. 5b). Induced

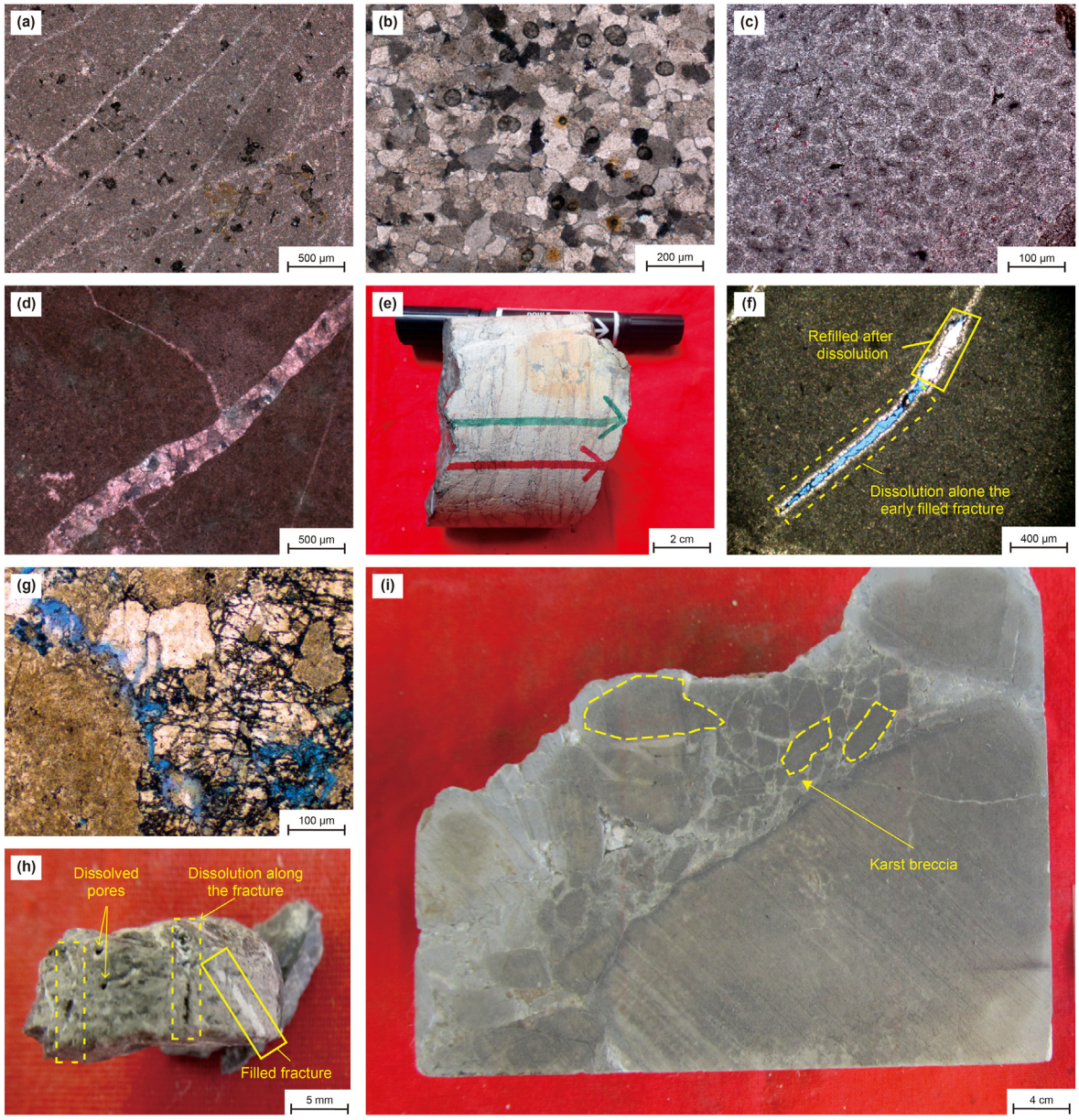

Fig. 2. Typical lithologies and reservoir space characteristics of the carbonate reservoirs on the western slope of the Bozhong Sag. (a) Microlite crystalline dolomite, well BZ22-1-A (4495.5 m), Liangjiashan Formation. (b) Fine crystalline dolomite, well BZ22-1-A (4597.0 m), Liangjiashan Formation. (c) Granular dolomite, well BZ22-1-A (4389.0 m), Majiagou Formation. Two stages of cementation can be observed; the first stage is circular dolomite granular cementation, the second stage is calcite filling intergranular pores. (d) Microlite crystalline limestone, well BZ22-1-A (4597.0 m), Liangjiashan Formation. Fracture filled with calcites and a few quartzes. (e) Warmkalk limestones, well BZ28-1-8D (3463.2 m), Gushan Formation. (f) Refilling of fractured veins after dissolution can be observed under the microscope, well BZ21-2-A (4873.0 m), Majiagou Formation. (g) Dissolve and expansion along the fracture can be observed under the microscope, well BZ28-1-6D (3700.0 m), Yeli Formation. (h) Dissolution pores and dissolution along the fractures can be observed in the core, well CFD2-1-2 (3442.5 m), Liangjiashan Formation. (i) Karst breccia observed in the core that breccia grains are dolomicrite, developing dissolved micropores, well BZ28-1-6D (3494.0 m), Majiagou Formation.

fracture is a type of wellbore failure, also called the drilling-induced tensile wall-fracture, caused by the vibration of drilling tools or squeezing the sidewall by mud (Brudy and Zoback, 1999). They were mainly symmetrically distributed dark stripes on the FMI image in the pinnate shape (Fig. 5a and b). In general, induced fractures can indicate the direction of the in-situ maximum principal stress (Aadnoy and Bell, 1998; Ye et al., 2019). Induced fractures on the southwestern slope of the Bozhong Sag indicate an NWW-trending in the maximum principal stress of the Bohai Bay Basin (Fig. 5c). In the literatures, there are examples of filled materials and effective (unfilled) fractures identified using image logging (Khoshbakht et al., 2009; Nie et al., 2013; Lai et al., 2018). The effective fractures display a dark sinusoidal curve as a result of the low resistance of the mud intrusion, while the filled or closed fractures show a bright colour, which is related to the filling of high-resistance minerals (Fig. 5a and b ; Barton and Zoback, 2002; Nie et al., 2013; Keeton et al., 2015).

Fracture orientation and dip. Image logging revealed that NW-SE (blue), NNE-SSW (red) and NNW-SSE (yellow) trending fractures developed in the carbonate buried-hill reservoirs of the southwestern slope of the Bozhong sag (Fig. 5d). NNW-trending fractures account for the majority of the reservoirs, accounting about 60% of the total number of fractures. Most fractures are dominated by medium-high dip angles ranging from 45° to 75° and account for approximately 70% of the total number of fractures (Fig. 5e).

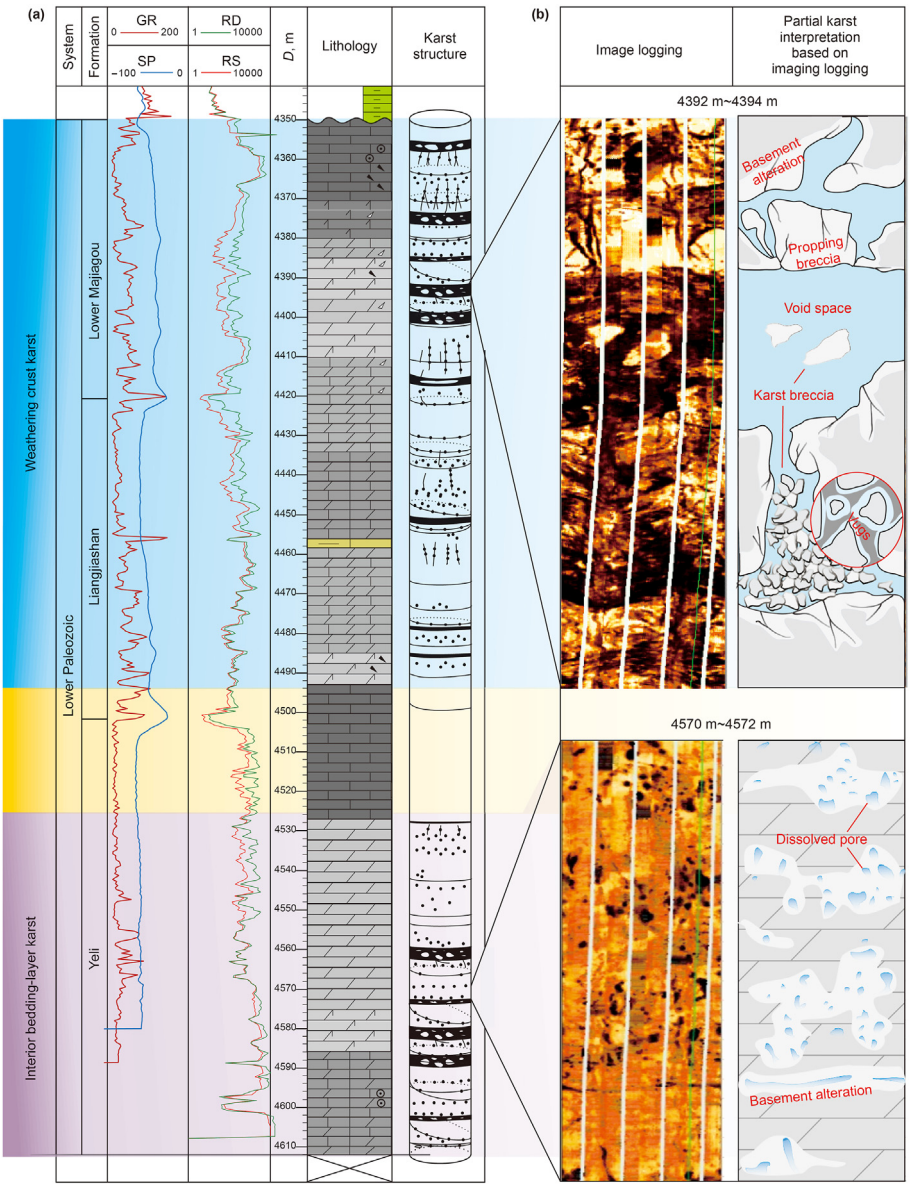

Fig. 3. (a) Schematic diagram of karst structure in drilling. (b) Partial karst structure interpretation based on image logging.

Fracture fill materials and apertures. The cores, thin sections, and image logs revealed both effective (unfilled) and filled fractures (Figs. 4 and 5). Among them, 18% of NNE-SSW, 64% of the NW-SE and 47% of the NNW-SSE trending faults are filled. There is a wide range of fracture widths calculated by image logging, ranging from 30 to 280 μm (Fig. 5e). The widths of the NNE-SSW trending fractures were larger, concentrated in the range of 200–280 μm, and the widths of the NW-SE and NNW-SSE trending fractures were primarily concentrated in the range of 50–140 μm. Considering that the tensional fracture generally has a larger width than the shearing fracture, we believe the NNE-trending fractures are related to the second family of fractures. Tectonic uplift and denudation generally result in more reserved fractures in the later stage, so the NW-trending corresponds to the first family of fractures and the NNW- trending corresponds to the third family of fractures.

4.3. Major, trace and rare-earth element

The data of major, trace, and rare earth elements of 15 calcite veins were measured using the *in situ* LA-ICP-MS method, excluded ablation points with weak signals. These calcite veins (C1 and C3) filled the two families of shearing fractures, respectively. Type C1 calcite corresponds to veins filled in NW- trending fractures, and type C3 calcite corresponds to veins filled in NNW-trending fractures. Suitable samples were not obtained because of the low degree of filling in the second family of tensile fractures. Meanwhile, we performed laser ablation of the host rocks (carbonate matrix) near the vein, including four crystalline limestones (Lim), four microlite dolomites (MD), and five fine crystalline dolomites (CD) samples. These data were used to discuss the properties of the diagenetic fluid in the dolomite matrix.

The major and trace elements included Na, Mn, Fe, and Sr (Table S2). The samples exhibited the following characteristics: (1)

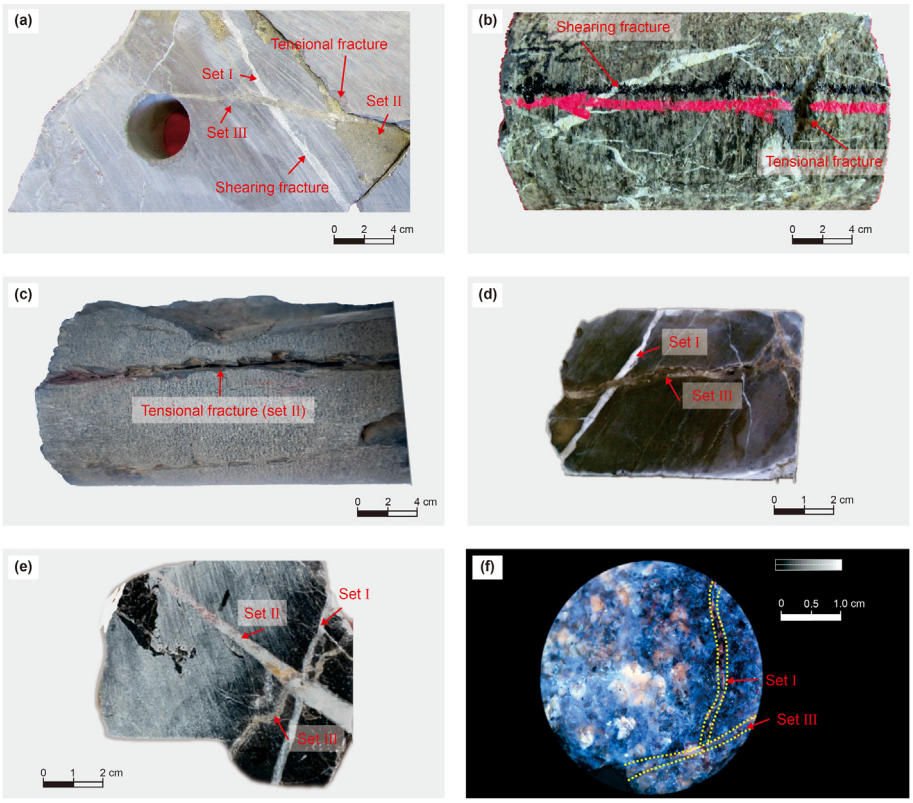

Fig. 4. Typical fracture characteristics of the carbonate reservoirs on the southwestern slope of the Bozhong Sag. (a) Two shear fractures (Family I and Family III) and one tensile fracture (Family II) can be observed in the core. The fractures of Family I are filled with fine crystalline calcites, the fracture of Family II was not filled, and the fracture of Family III is filled with argillaceous calcites. Well BZ28-1-8D (3440.0 m). (b) The shearing fracture filled with calcite veins and the tensional fracture are not entirely filled, Well BZ28-1-7 (3217.0 m). (c) An unfilled tensional fracture observed in the core, Well BZ28-1-7 (3220.0 m). (d) The two families of fractures cut each other and filled the calcite veins of two occurrences respectively, Well CFD2-1-2 (3706.0 m). (e) The three families of fractures cut each other and filled with calcite veins respectively. Well CFD2-1-2 (4903.0 m). (f) Under the UV microscope, tectonic fractures are visible in the thin sections. Fractures show strong fluorescence inside and around them, indicating they were effective. Well BZ22-1-A (4832.0 m).

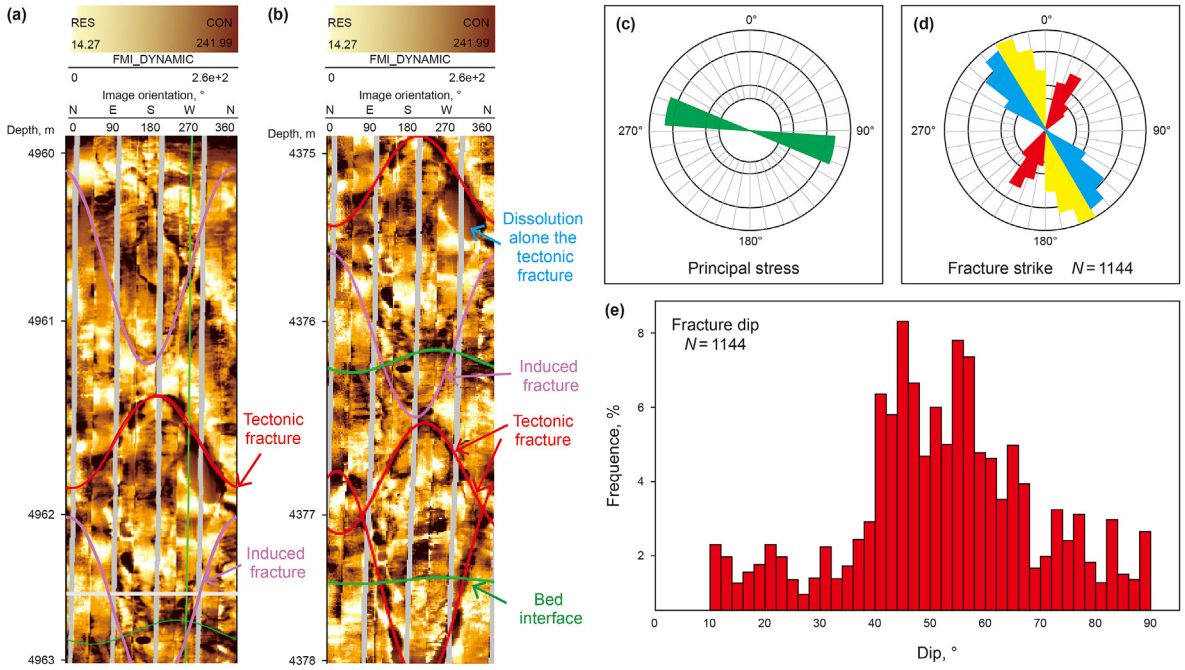

Fig. 5. Natural fractures were interpreted from the image logs of the carbonate basement of the southwestern slope of the Bozhong Sag. Red curves represent tectonic fractures. Pink curves represent induced fractures. Green curves represent the bed interface. (a) Induced fractures and tectonic fractures from well BZ21-2-A. (b) Induced fractures and tectonic fractures from well BZ22-1-A. Note the dissolved pores developed along the fracture (Blue curves). (c) Rose plot of induced fractures shows the NWW- trending maximum principal stress. (d-e) Fracture strike and dip calculated from image logs.

The CD (227.38–494.55 ppm) exhibited lower Na levels than that in Lim (277.82–640.00 ppm) and MD (495.55–669.20 ppm). The calcite veins C1 and C3, exhibited lower Na levels than those in matrix samples, and C1 (34.02–75.75 ppm) exhibited higher Na levels than C3 (9.14–66.96 ppm). (2) The CD (64.18–116.96 ppm) exhibited higher Mn levels than that in Lim (41.43–62.71 ppm) and MD (56.86–72.19 ppm). C1 (56.86–187.56 ppm) exhibited similar Mn levels to those in MD and CD, but the C3 (177.49–747.60 ppm) exhibited higher Mn levels than those in the other samples. (3) MD (1041–1679 ppm), CD (1574.53–2495.35 ppm) and C1 (1105.31–2053.42 ppm) exhibited similar Fe levels, but C3 (2133.24–11788.53 ppm) exhibited higher Fe levels than that in other samples. (4) CD (760.16–1176.43 ppm) exhibited lower Sr levels than that in MD (1041–1679.78 ppm). C3 (107.60–274.71 ppm) exhibited lower Sr levels than that in C1 (281.54–443.92 ppm), and the vein samples (C1 and C3) exhibited obviously lower Sr levels than those in the carbonate matrix samples (Lim, MD, and CD).

In previous studies, rare earth elements (REE) have been widely used as geochemical tracers. Numerous studies have selected "Chondrites" (Masuda et al., 1973; Yurimoto et al., 1990), "North American shale composite (NASC)" (Gromet et al., 1984) or "Post-Archaean Australian average shale (PAAS)" (Schwinn and Markl, 2005) as the normalized standard to process the REE data. However, the samples selected in this study seem to be more closely related to seawater than the previously mentioned standards; therefore, we chose the REE of the seawater as the normalized standard. Many studies on carbonate diagenetic fluids have normalized REE values using this standard and have been well interpreted (Nothdurft et al., 2004; Wang et al., 2014). The REE composition of the seawater was obtained from a study by Kawabe et al. (1998). Owing to the exextremely low REE content of the seawater, its REE concentration was amplified 10^6 times before normalisation. The parameters characterizing REE composition were ΣREE, light rare earth element (LREE)/heavy rare earth element (HREE), $(Eu/Eu^*)_{SN}$ and $(Ce/Ce^*)_{SN}$. The results are presented in Table S3. All the samples exhibited low REE content, and the ΣREE was in the range of 4.27–32.34 ppm, with an average of 12.05 ppm ($n = 28$). This was consistent with carbonate rocks exhibiting low REE (Nothdurft et al., 2004). The samples had the following characteristics: (1) The matrix samples of the three lithofacies exhibited similar characteristics and a strong positive Ce anomaly ($(Ce/Ce^*)_{SN\text{-}average\text{-}Lim} = 6.94$, $n = 4$; $(Ce/Ce^*)_{SN\text{-}average\text{-}MD} = 7.79$, $n = 4$; $(Ce/Ce^*)_{SN\text{-}average\text{-}CD} = 6.92$, $n = 5$), no Eu anomaly ($(Eu/Eu^*)_{SN\text{-}average\text{-}matrix} = 0.93$, $n = 13$), and relative enrichment of light rare earth elements ($LREE/HREE_{average} = 4.09$, $n = 13$). The difference between the three types of matrix samples was reflected in the ΣREE. The ΣREE of CD was significantly lower than those of Lim and MD ($\Sigma REE_{average\text{-}Lim} = 15.25$, $n = 4$; $\Sigma REE_{average\text{-}MD} = 22.46$, $n = 4$; $\Sigma REE_{average\text{-}CD} = 8.00$, $n = 5$). (2) C1 exhibited a lower ΣREE than that of the Lim and MD samples; C1 and carbonate matrix samples (Lim, MD, and CD) showed the same enrichment of HREE ($LREE/HREE_{average\text{-}C1} = 2.34$, $n = 5$), and the Eu of the C1 samples showed no abnormality ($(Eu/Eu^*)_{SN\text{-}average\text{-}C1} = 0.99$, $n = 5$). The average ΣREE of C3 was 10.22 ($n = 10$); C3 samples had a balance of light and heavy rare earth elements ($LREE/HREE_{average\text{-}C3} = 0.97$, $n = 10$). The Ce of the C3 samples also showed a positive anomaly but was the lowest level compared to the other sample types ($(Ce/Ce^*)_{SN\text{-}average\text{-}C1} = 5.91$, $n = 5$; $(Ce/Ce^*)_{SN\text{-}average\text{-}C3} = 5.03$, $n = 10$). The Eu of the C3 samples showed no anomaly ($(Eu/Eu^*)_{SN\text{-}average\text{-}C3} = 0.98$, $n = 10$).

4.4. Carbon and oxygen isotopes

Carbon and oxygen isotope analyses were carried out on the carbonate matrix of the reservoirs, and the calcite filled in the fractures developed in these matrix samples. The values of 37 matrix samples (limestone and dolomite) and 23 vein samples (calcite) were measured (some vein samples could not be detected owing to the small amount of content). The results are shown in Table S4.

The carbonate matrix samples showed a narrow carbon isotope distribution, while the oxygen isotope was relatively negative. The range of $\delta^{13}C$ is −3.68‰~ −1.90‰, and the average is −0.53‰ ($n = 37$). The range of $\delta^{18}O$ is −17.90‰~ −4.80‰, and the average is −10.02‰ ($n = 37$). Among them, the $\delta^{13}C$ of the Lim is distributed in the range of-1.39‰–0.91‰, with an average value of −0.64‰ ($n = 10$), and $\delta^{18}O$ is distributed from −0.60‰ to-11.85‰, with an average value of −9.85‰ ($n = 10$). The $\delta^{13}C$ of MD ranged from −3.11‰ to 0.81‰, with an average of −0.31‰ ($n = 9$), and $\delta^{18}O$ ranged from −10.40‰ to −17.90‰, with an average of −13.286‰ ($n = 9$). The $\delta^{13}C$ of CD ranged from −3.61‰ to 0.86‰ with an average of −0.70‰ ($n = 16$), and $\delta^{18}O$ ranged from −4.80‰ to −12.14‰ with an average of −8.34‰ ($n = 16$). For the calcite veins filled in the fractures, the $\delta^{13}C$ of the C1 ranged from −3.33‰–5.81‰, with an average of 1.60‰ ($n = 9$), and the $\delta^{18}O$ ranged from −7.03‰ ~-20.51‰, with an average of −15.13‰ ($n = 9$). The $\delta^{13}C$ of the C3 ranged from −2.40~-0.91, with an average of −1.25‰ ($n = 14$), and the $\delta^{18}O$ ranged from-10.06‰ ~-21.48‰, with an average of −17.26‰ ($n = 14$).

4.5. Strontium isotope

$^{87}Sr/^{86}Sr$ analysis of 30 carbonate matrix samples and 16 calcite samples filled in the fractures of the matrix were measured (Table S4).

The $^{87}Sr/^{86}Sr$ ratios of the carbonate matrix samples range from 0.709079 to 0.729942 with the average was 0.711691 ($n = 30$). The $^{87}Sr/^{86}Sr$ ratio of the Lim ranges from 0.709079 to 0.716018 with an average of 0.710147 ($n = 8$). However, 90% of the limestone samples ranged from 0.709079 to 0.709476, with an average of 0.709308 ($n = 7$). In the dolomite samples, the $^{87}Sr/^{86}Sr$ ratio ranged from 0.709190 to 0.716797, with an average of 0.711409 ($n = 21$). The $^{87}Sr/^{86}Sr$ ratio of the MD was 0.710120–0.711582, with an average of 0.710260 ($n = 13$), and the $^{87}Sr/^{86}Sr$ ratio of the CD ranged from 0.709853 to 0.716797, with an average of 0.713268 ($n = 8$). The $^{87}Sr/^{86}Sr$ ratio of the fine crystalline dolomite (CD) was significantly higher than that of the microlite dolomite (MD).

The $^{87}Sr/^{86}Sr$ ratio of the calcite filled in the fractures ranged from 0.709282 to 0.720779. Among them, the $^{87}Sr/^{86}Sr$ ratio of the C1 ranged from 0.709282 to 0.713468, with an average of 0.711397 ($n = 6$). The C3 ranged from 0.713001 to 0.720779, with an average of 0.716062 ($n = 10$). The $^{87}Sr/^{86}Sr$ ratio of the C3 was significantly higher than that of the C1 and matrix samples.

5. Discussion

5.1. Properties of diagenetic fluids

Evaluation of data validity. The loss of Na and Sr and the enrichment of Fe and Mn are affected by the meteoric water cycle during the later stages of carbonate sedimentation (Brand and Veizer, 1980; Huang, 1997). Therefore, the Mn/Sr ratio of the samples can be used as an indicator of diagenesis and alteration. It is believed that Mn/Sr < 2–3 indicates that the sample has not undergone diagenetic alteration (Derry et al., 1989; Kaufman et al., 1993; Yan et al., 2005; Huang et al., 2008). The Mn/Sr ratios in this study were all less than 2 (Table S2), indicating that the carbonate samples were unaffected by diagenetic alteration.

Matrix (Dolomite). Tracing the source of dolomitisation fluids using normalized REE patterns has been widely used in the past

studies. Common dolomitisation fluids include seawater or fluids derived from seawater (Friedman and Sanders, 1967; Hsü and Schneider, 1973; Saller, 1984), highly saline brine (Melim and Scholle, 2002), mixed water (Badiozamani, 1973), and hydrothermal fluids (Qing and Mountjoy, 1994; Davies and Smith Jr, 2006). Ancient limestone records REE signatures of contemporary seawater (Nothdurft et al., 2004). The REE patterns of all matrix samples had consistent features after seawater normalisation (Fig. 6), including positive Ce anomalies and HREE enrichment. The Ce anomaly, which is particularly negative, is a characteristic of seawater (Sholkovitz and Shen, 1995; Azmy et al., 2011). However, the seawater-normalized REE patterns in this study show positive Ce anomalies ($(Ce/Ce^*)_{SN} > 1$) in all samples (Fig. 6). Considering the factors that influence Ce anomalies, such as water depth, salinity, and oxygen levels, Ce tends to be more enriched in marine carbonate compared to its REE neighbors lanthanum (La) and praseodymium (Pr) (Sholkovitz et al., 1994; Shields and Stille, 2001). Therefore, the positive Ce anomaly after seawater normalisation indicates seawater which is different from conventional characteristics normalized by other standards, such as PAAS and NASC. The normalized REE patterns of the two types of dolomite-samples (MD and CD) were compared with those of the limestone samples (Lim). These three sample types exhibited consistent features (Fig. 6), indicating that the two types of dolomite have similar dolomitisation fluids associated with seawater or seawater-derived fluids. ΣREE of Lim and MD samples were in the same range, while the ΣREE of CD samples was relatively low (Table S3, Fig. 6), indicating that the CD samples were accompanied by REE dilution during the dolomitisation process (Yang et al., 2018; Xiang et al., 2020).

The Fe and Mn elements are lacking in seawater but are enriched in diagenetic pore-water and atmospheric freshwater, and with the enhancement of diagenesis, the contents of Fe and Mn tend to increase. Sr is an essential trace element in seawater and seawater-derived fluids, and Sr tends to be lost with an increase in diagenetic intensity. Na directly reflects the salinity of the diagenetic fluid (Zhu et al., 2020). High Fe and Mn contents are effective indicators for identifying burial dolomite and are more effective than Sr and Na contents (Wierzbicki et al., 2006). The MD and Lim samples have similar Na and Sr element contents and are characterized by high levels, indicating that a high-salinity environment may have formed MD dolomite. Therefore, the MD dolomite can be interpreted as dolomite formed during the penecontemporaneous Sabha process. The Sr and Na contents of the CD samples were much lower, and the Mn and Fe contents were higher than those in Lim and MD samples. This was attributed to recrystallisation during shallow burial.

Additionally, C, O, and Sr isotopes are commonly used to identify the source of dolomized fluids, and the properties of the diagenetic fluid strongly affect the C and O isotopes of marine carbonate rocks. The carbon and oxygen isotopes of most matrix samples fall within the range of marine carbonate rocks reported by Veizer and Hoefs (1976), indicating that the diagenetic fluids were derived from seawater (Fig. 7). The concentration of strontium is high in seawater, and the oceanic retention time of strontium (approximately 106 yr) is much longer than that of seawater (approximately 103 yr); therefore, the $^{87}Sr/^{86}Sr$ ratio of seawater is uniform throughout the oceans over a fixed range of geological periods (Elderfield et al., 1982; Jones and Jenkyns, 2001). The $^{87}Sr/^{86}Sr$ ratio of seawater is mainly influenced by strontium from continental

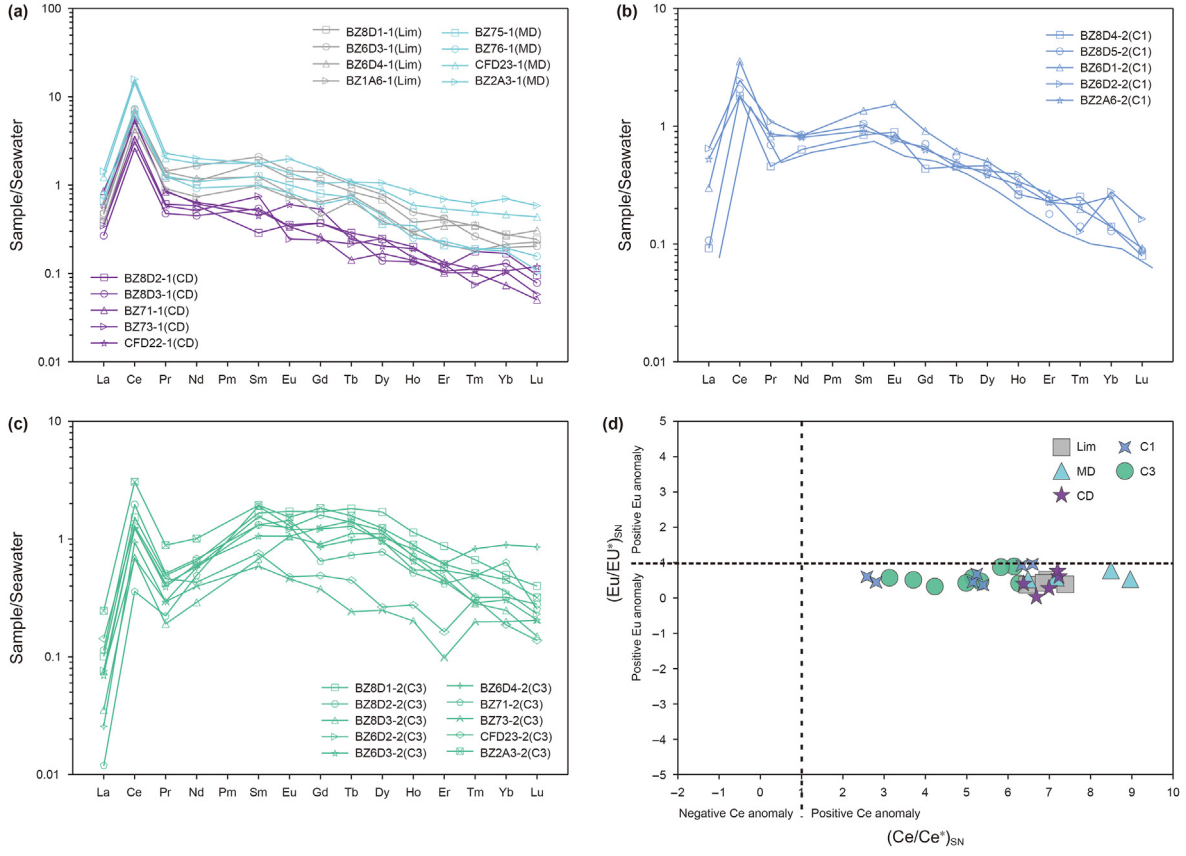

Fig. 6. Sea water- normalized rare-earth element (REE) patterns. The detailed results of each sample are shown in Table S2. (a) Three types of carbonate matrix samples. (b) The calcite veins filled in NW- trending fractures (C1). (c) The calcite veins filled in NNW- trending fractures. (d) Scatter diagram of Eu–Ce anomaly for matrix and vein samples.

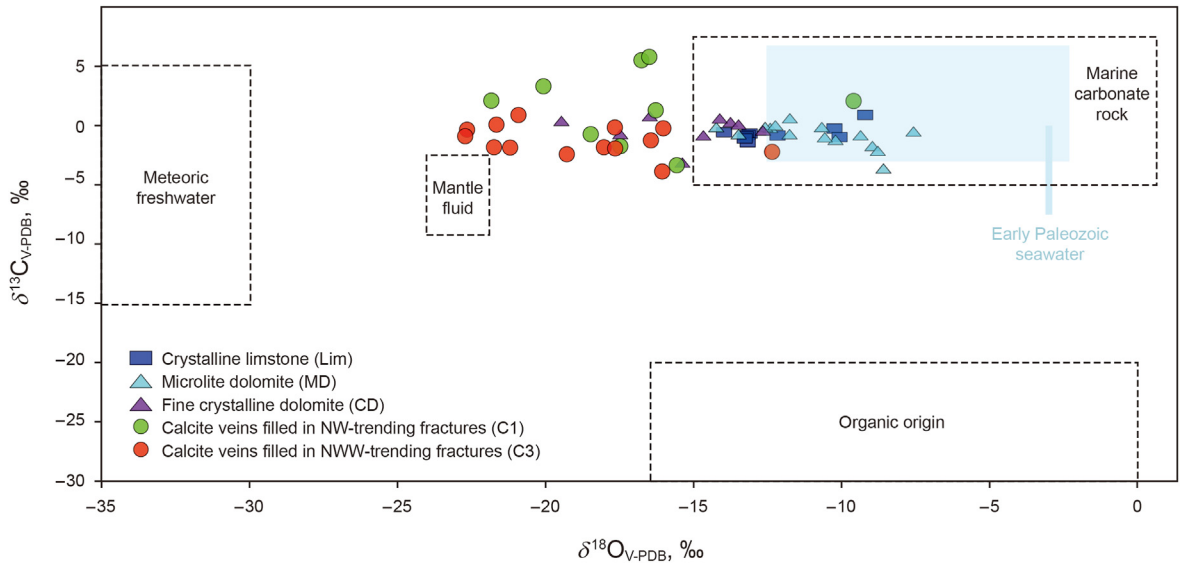

Fig. 7. Carbon and oxygen isotopes characteristic of the matrix and fracture-filled calcites. The marine carbonate rock data refer to Veizer and Hoefs (Veizer and Hoefs, 1976) and Hudson (Hudson, 1977). Isotope compositions of meteoric freshwater are from Hoefs (Hoefs, 1997) and Zheng (Zheng et al., 2007). The mantle fluid data refer to Hugh P. Taylor (Taylor, 1974), Hugh P. Taylor, and Simon M. F. (Taylor and Sheppard, 1986). The data of organic origin are from Deines (Deines and Peter, 1980) and Hoefs (Hoefs, 1997). The layout was modified by Liang (Liang et al., 2019).

crust (high $^{87}Sr/^{86}Sr$) and upper mantle (low $^{87}Sr/^{86}Sr$) (Elderfield et al., 1982). However, the $^{87}Sr/^{86}Sr$ ratios of some dolomite samples were higher than those of the Early palaeozoic seawater and limestone samples (Fig. 8). Based on the above theory, the high $^{87}Sr/^{86}Sr$ ratio of carbonate may be ascribed to diagenetic fluid that migrated through siliciclastic deposits and then modified carbonates. Alternatively, during the syndepositional stage, supratidal flats occasionally form gypsum salt deposits, and the high $^{87}Sr/^{86}Sr$ ratios of MD dolomite may be related to the presence or dissolution of gypsum salt. The $^{87}Sr/^{86}Sr$ ratios of CD dolomite were higher than those of seawater and microlite dolomite (Fig. 8) and similar to burial dolomite (Spotl and Pitman, 1998), so we inferred that the CD dolomite was formed by recrystallisation in the shallow burial environment. Burial dolomitisation resulted in the recrystallisation of the "seed crystal" of penecontemporaneous microlite dolomite and the formation of fine crystal dolomite with a good crystal shape. In the shallow burial stage, external terrestrial fresh water rich in crust-derived radioactive ^{87}Sr was transported vertically into the Ordovician carbonates through the Ordovician weathering crust and participated in the formation of CD dolomite. Additionally, studies have shown that recrystallisation, mixed terrestrial freshwater, and temperature increases in buried environments all contribute to the negative drift of $\delta^{18}O$ (Baertschi, 1976). This also explains why the $\delta^{18}O$ of the CD samples is significantly more negative than that of the Lim and MD samples. The ΣREE, Mn, and Fe elements of CD were lower than that of Lim and MD samples

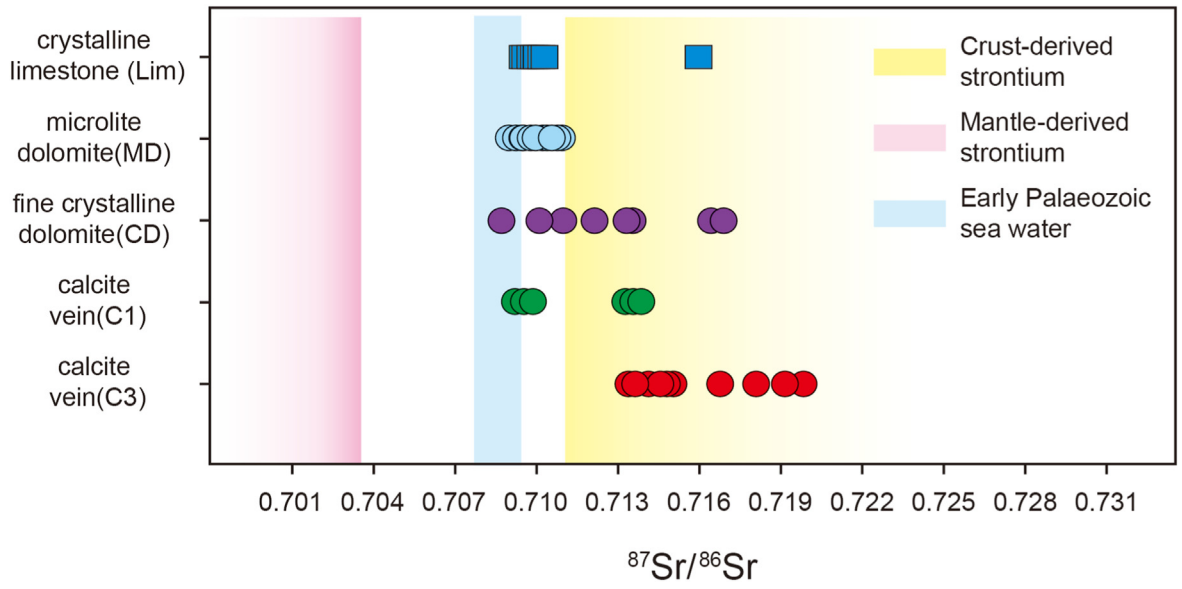

Fig. 8. $^{87}Sr/^{86}Sr$ characteristic of the matrix and fracture-filled calcites. The range of crust-derived strontium, mantle-derived strontium (Palmer and Edmond, 1989) and the early palaeozoic seawater (Veizer and Hoefs, 1976) are indicated.

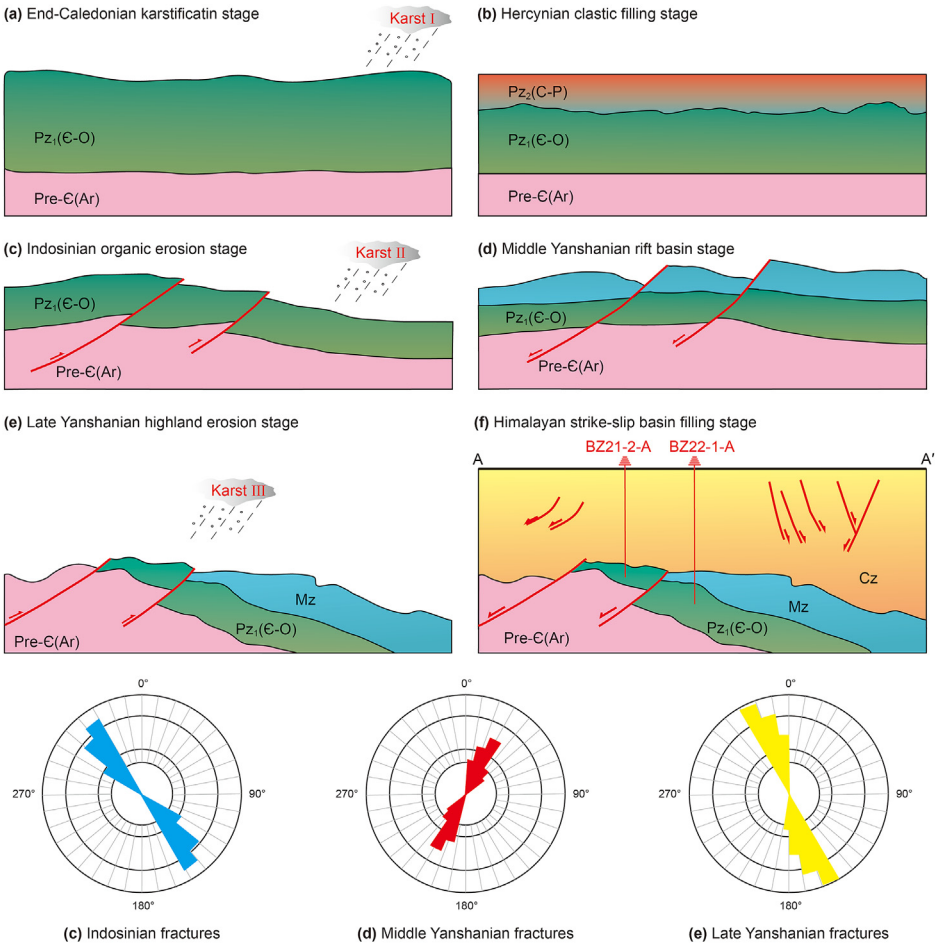

Fig. 9. Diagram showing the tectonic evolution of the southwestern Bozhong Sag (profile position seen in Fig. 1c).

(Tables S2 and S3), indicating that the effect of terrestrial freshwater in CD is slightly higher than that in Lim and MD, which also corroborates this view.

In summary, the diagenetic fluid of MD and CD dolomites is seawater. MD dolomite was formed in a tidal-flat evaporative environment with high salinity. In contrast, CD dolomite was formed by recrystallisation of MD dolomite in a shallow burial environment, during which a small amount of terrigenous fresh water rich in radioactive ^{87}Sr continental crust was mixed.

Vein (Calcite). The geochemical analysis of calcite veins obtained from the two families of fractures showed a significant difference, indicating that the diagenetic fluid properties of the two types of veins may differ. The following paragraphs discuss the diagenetic fluid properties of C1 and C3 samples based on the isotopes and rare earth, major, and trace elements.

The average value of $(Eu/Eu^*)_{SN}$ in carbonates is approximately 0.233 (Turekian and Wedepohl, 1961) and 0.411 in the crust (Mason, 1966). Eu tends to be enriched in mantle-derived materials and hydrothermal fluids. Therefore, when these two types of materials are mixed with diagenetic fluid, the REE of rocks will show a positive Eu anomaly ($(Eu/Eu^*)_{SN} > 1$) (Macrae et al., 1992). The REE of both C1 and C3 samples show slightly negative or no Eu anomalies (Fig. 6d, Table S3), therefore, we can rule out the source being mantle-derived material or hydrothermal diagenetic fluid. The C1 samples show the right deviation on the normalized pattern, indicating enrichment of HREE, accompanied by a positive Ce anomaly (Fig. 6b, Table S3). These features were highly similar to those of the seawater-derived carbonate matrix previously discussed (Fig. 6a). Therefore, it was inferred that the diagenetic fluids of the C1 type calcites are related to the carbonate matrix. This means that the product of cabonate matrix dissolution and re-precipitation under internal runoff karst water (such as rainfall) (Reid et al., 2013). The REE normalized pattern of the C3 samples is flat, with approximately equal light and heavy rare earth element contents. The positive anomaly of Ce was significantly lower in the C3 samples compared with that in the C1 and carbonate matrix samples. These features are consistent with the REE characteristics of carbonate rocks associated with fresh water proposed by Hu et al. (2010). However, studies have demonstrated that the ΣREE of fresh water is extremely lower than that of rocks (Aubert et al., 2002), but the ΣREE of the C3 samples was not much lower than that of carbonate matrix samples. This phenomenon can be explained by the allogenic recharge of lateral freshwater flow (such as river water) with high mud content which also participates in the formation of calcite veins through karstification. Mud with high REE neutralized the low REE of fresh water. This diagenetic fluid assemblage was also supported by the high argillaceous content of C3 calcite.

C1 samples exhibited higher Na–Sr and lower Mn–Fe contents compared with C3 samples, indicating that the diagenetic fluid of type C1 calcite had higher salinity and an enclosed diagenetic environment. The low concentrations of Na and Sr and high concentrations of Mn and Fe in the C3 calcite represent the source of the diagenetic fluid of terrigenous freshwater.

$^{87}Sr/^{86}Sr$ ratio was strongly influenced by continental crust strontium for both the C1 and C3 samples. It is speculated that it is influenced by atmospheric freshwater rich in crust heavy strontium, and it can be ruled out the related to deep mantle fluid. Most of the $^{87}Sr/^{86}Sr$ in C1 samples are between the range of strontium from crust-derived and seawater, indicating that they were derived from the dissolution of the host rock after karstification. The C3 samples are within the range of crust-derived$^{87}Sr/^{86}Sr$, indicating that the diagenetic fluid is controlled by terrigenous freshwater.

$\delta^{18}O$ is extremely sensitive to temperature. Previous studies have shown hydrothermal fluids and atmospheric freshwater exhibit very low $\delta^{18}O$ values (Keith and Weber, 1964). The increase in temperature in the burial environment also caused $\delta^{18}O$ to be negative. The $\delta^{18}O$ values of the calcite veins in this study were strongly negative. The REE and $^{87}Sr/^{86}Sr$ discussion has excluded the influence of deep mantle fluid and hydrothermal conditions in producing the negative oxygen isotope; therefore the presence of the isotope can only be caused by either the atmospheric freshwater or buried environment. The $\delta^{13}C$ of C1 samples was similar to or slightly higher than that of host rocks when comparing the vein and matrix samples; therefore, it is verified that the type C1 calcites caused by the dissolution of the host rock and re-precipitation. The $\delta^{13}C$ values of the C3 samples were lower than those of the host rocks. We speculate that this might be due to the terrestrial fresh water which has more ^{12}C of soil, resulting in the negative $\delta^{13}C$ in type C3 calcites.

Keith et al. (1964) proposed a formula for distinguishing marine carbonate rocks ($Z > 120$) from freshwater carbonate rocks ($Z < 120$) using the $\delta^{13}C$ and $\delta^{18}O$ of carbonate rocks to calculate palaeosalinity (Z). The formula is as follows:

$$Z = 2.048 \times (\delta^{13}C_{(\%PDB)} + 50) + 0.498 \times (\delta^{18}O_{(\%PDB)} + 50)$$

Although Keith proposed a formula applicable only to the Jurassic and later strata, previous experience in the Tarim, Qaidam, and Bohai basins of China shows that the formula applies to older strata (Wang, 2000). The Z values of C1 samples range from 107.39 to 125.60, with an average of 116.749 ($n = 9$), indicating the high salinity similar to marine carbonate rock. And the Z values of C3 calcite range from 106. 04 to 113.53, with an average of 109.736 ($n = 13$), and the salinity was low, indicating freshwater facies carbonate rock.

5.2. Formation of the three fracture families

The previous results show that the study area mainly produces three families of fractures. The first is the NW-trending extrusion fractures, the second is the NNE-trending tensile fractures, and the third is the NNW-trending extrusion fractures. To clarify the forming period of these families of fractures, the primary tectonic evolution process of the study area was reconstructed by the seismic balance profile combined with the regional tectonic evolution background of the North China plate.

(1) After the lower Palaeozoic carbonate rocks were deposited, the North China platform was uplifted as a whole by the Caledonian movement and entered a denudation period of nearly 130 Ma (Zhai et al., 2011; Xiong et al., 2022). Upper Ordovician, Silurian, and Devonian deposits were absent in the study area (Fig. 9a).
(2) After entering the Hercynian period, the uplift stopped, and Carboniferous and Permian strata were deposited in the study area (Fig. 9b).
(3) In the Indosinian orogeny, the tectonic regime transitioned significantly. The eastern part of the North China Plate was subjected to intense tectonic compression from the Qinling-Dabie orogenic belt in the south and the Central Asian orogenic belt in the north (Kovalenko et al., 2004; Hou et al., 2020). The Bozhong area is a tectonic plateau formed by a nearly east-west thrust (Yu et al., 2002), and a series of NW-trending shear fractures are generated. The appearance of the first family of extrusion fractures is consistent with that. Simultaneously, the east-west direction compressive stress also caused a second uplift of the crust, which resulted in the previously deposited Carboniferous and Permian denuded and the lower Palaeozoic re-exposed to the surface (Fig. 9c)
(4) In the middle Yanshanian orogeny, the Tan-Lu deep fault running through the eastern part of the North China plate, and the back-arc spreading of the Pacific Plate subduction formed a series of NNE-trending rift basin and the related horst (Fig. 9d; Zheng and Dai, 2018). The second family of NNE-trending tensile faults was formed in this tectonic background.
(5) At the end of the Mesozoic, the angle and rate for the subduction of the Pacific Plate to the Eurasian Plate changed dramatically, which triggered the mantle diapir and caused the destruction of the North China Craton (Li et al., 2010; Zhang et al., 2014). In addition, the NE-SW trending left-lateral shear stress field was formed by the oblique convergence between plates, resulting in regional unconformity and related thrust faults, corresponding to the third family of extrusion fractures in the study area. In the mean time, fault block tilting occurred in the hills buried in the study area under the compressive stress (Ye et al., 2022). The Mesozoic at the highly-seated portion of the buried hill was denuded by uplift, and the lower Palaeozoic was re-exposed to the surface for the third time. In contrast, the Mesozoic at the relatively lower part of the buried hill was not denuded (Fig. 9e).
(6) Subsequent to the Cenozoic, the Bohai Bay basin became a large strike-slip and pull-apart basin under the continuous subduction of the Pacific plate (Cai, 2001; Hu et al., 2001). Some pre-existing faults in the basement are partially reactivated, and new fractures related to strike-slip occur (Allen et al., 1997; Huang et al., 2012; Liang et al., 2016). The horst of the basement is gradually buried to form a unique buried hill trap (Fig. 9f).

5.3. Genesis mechanism of the polyphase fracture-related karst reservoirs

Herein, based on the karstification occurred in different tectonism backgrounds, the carbonate karstification reservoirs are classified into three types. One is the classic hydraulic stratified karstification in large-scale cratonic drainage basins, such as Ordovician Ordos Basin (Wang and Al-Aasm, 2002; Xiong et al., 2022). The second is fracture-related karstification in the rifting horsts of the extensional tectonic regime with allogenic recharge, such as the Cenozoic Suez Rift Basin (Bosworth et al., 2014; Radwan et al., 2021). The third is fracture-related karstification in the highland of thrusting setting with autogenic recharge, such as Ordovician Tarim Basin (Fu et al., 2017; Li et al., 2019). The study area successively experienced cratonic erosional unconformities, thrusting highlands, and rifting horst settings. Consequently, the carbonate basement developed polyphase karstification (Fig. 9), which included Caledonian karstification in cratonic erosional

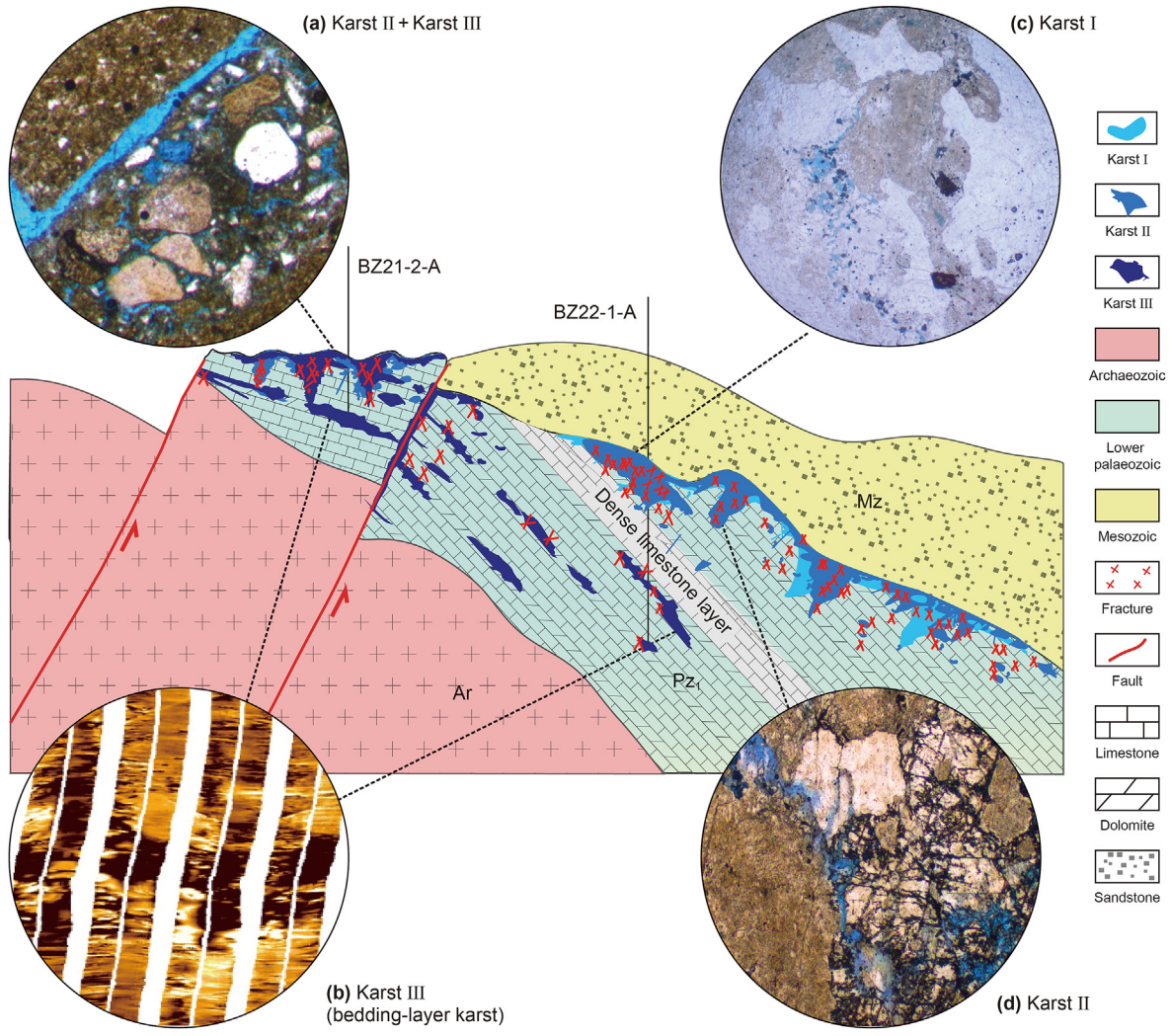

Fig. 10. Formation model of polyphase fracture-related karstification reservoirs in the lower Palaeozoic carbonate buried hill on the southwestern slope of the Bozhong Sag. (a) Indosinian and Late Yanshanian fracture-related karstifications shown under the microscope; (b) Interior bedding-layers karst of the late Yanshanian inside the buried hill shown by image logging; (c) Caledonian non-fracture related karstification shown under the microscope; (d) Indosinian fracture-related karstification shown under the microscope.

Table 1
Main characteristics of the polyphase karstification in the lower Palaeozoic carbonate buried hill on the southwestern slope of the Bozhong Sag.

Kastification phase	Karst I	Karst II	Karst III
Forming period	Caledonian	Indosinian	Yanshanian
Tectonic background	Cratonic erosional unconformity,	Thrusting highland	Rifting horst
Fluid properties of karst products	/	Autogenic recharge from rainfall (internal diffuse flow)	allogenic recharge predominated by external runoff
Reservoir space	Dissolution pores and caves	Dissolution pores and caves; tectonic fractures; dissolution fractures	Dissolution pores and caves; tectonic fractures; dissolution fractures
Preserve position	Mesozoic coverage area	Non Mesozoic coverage area/Mesozoic coverage area	Non Mesozoic coverage area/Mesozoic coverage area (only bedding layer karst)

unconformity setting (Karst I), Indosinian karstification in thrusting highland background (Karst II), and Yanshanian karstification in extensional rift regime (Karst III).

The earliest Caledonian karst was non-fracture-related karstification in a large-scale cratonic drainage basin, which occurred in exotic fine detrital caves or pore-fills. This type of karstification is well preserved in Ordos Basin, western of North China Block (Xiong et al., 2019). However, in OBBB, it is suffered intense erosion and tectonic damage. The secondary Indosinian karst is a compressional tectonic fracture-related karstification in the highlands of the thrusting regime, which is characterized by straight sparry calcite fracture fills. The latest Yanshanian karst was an extensional tectonic fracture-related karstification in a rifting horst setting and was recorded in irregular micritic calcite fracture fills. The fluid-forming Indosinian straight sparry calcite fracture fills are of autogenic recharge from rainfall (internal diffuse flow) with an exchange between the matrix and conduits; therefore, the matrix geochemical information can be determined from the fills.

However, the fluid forming the Yanshanian irregular micritic calcite fracture-fills is due to allogenic recharge mainly by external runoff. The fills mixed with exotic detrital impurities resulted in dark brown contamination.

The interpretation of the karst reservoir based on image logging shows that fracture-related karst in the study area includes surface weathering crust karst and interior bedding layer karst, which is divided by a dense limestone layer in the middle (Fig. 3b). Its lithological selectivity makes dolomite more susceptible to fracture and related dissolution. On the one hand, dolomite has more primary pores (Purser et al., 1994) and is more brittle than limestone (Mogi, 1971), making dolomite more prone to fractures. On the other hand, this is due to the different dissolution rates of limestone and dolomite in different geologic fluid settings: in an open system, the dissolution capacity of limestone is much greater than that of dolomite, and after entering the burial environment, with the increase in ambient temperature and pressure, the dissolution rate of dolomite becomes higher than that of limestone (She et al., 2016; Ye et al., 2020a,b). In the late Yanshanian orogeny, the buried hill was affected by compressive stress. The Mesozoic strata at the high settlement of the buried hills was denuded by the extruding uplift and caused a fault block in the lower Palaeozoic strata. Water flowing from the strata cross-section can enter the interior of the buried hill along the dolomite layer with numerous fractures and original pores, causing the dissolution and formation of the bedding layer karst.

Spatially, polyphase karstification acted on different portions of the buried hill. Affected by the local tectonic uplift caused by compression stress in the late Yanshanian orogeny, some Palaeozoic strata of the highly-seated portion of the buried hills are directly unconformable under the Cenozoic strata, and Mesozoic strata are completely denuded in these portions (Fig. 9e). In the other portions, lower Palaeozoic strata overlie Mesozoic strata (Fig. 9e). This difference in contact relationship also contributes to differences in karstification occurrence. The higher-seated portion of the buried hill, which no Mesozoic covered was mainly affected by the Indosinian karstification (Karst II) and late Yanshanian karstification (Karst III) (Fig. 10 a and b). The Caledonian non-fracture-related karstification (Karst I) was not preserved due to uplifting and denudation. The lack of surface exposure during the late Yanshanian period resulted in the records of the first two karst phases (Karst I and II), and the bedding karst from Karst III being preserved in the lower-seated portion of the Mesozoic coverage area (Fig. 10c and d). Based on the above discussions, the following table (Table 1) can be used to summarize the main characteristics of the three phases of karstification.

The discussions indicate that the lower Palaeozoic carbonate reservoirs in the southwestern slope of the Bozhong Sag were formed by a layered dolomite distribution controlled by the sedimentary environment and polyphase fracture-related karstification reconstructions. The widely developed tidal flat facies of the carbonate platform and epeiric sea controlled the distribution of dolomite and laid the foundation for forming the reservoirs. The superimposed transformation of polyphase karstifications formed reservoir space, and the effect of the polyphase karstification was the main reason for the difference in reservoir quality between the Mesozoic and non-Mesozoic coverage area on the southwest slope of the Bozhong Sag.

6. Conclusions

The polyphase fracture-related karst basement reservoirs of the lower Palaeozoic carbonate on the southwestern slope of the Bozhong Sag in OBBB are mainly developed in the dolomite strata. The source of the dolomite diagenetic fluid was mainly seawater in the penecontemporaneous period.

Three families of fractures occurrence in the reservoirs. The NW-trending and NNW-trending shear fractures are mainly related to the two tectonic compressions in the Indosinian orogeny and late Yanshanian orogeny. In contrast, the NNE-trending tensile fractures are related to the middle Yanshanian extension movement. Calcite veins were filled in three families of fractures. The geochemistry of the calcite veins filling these fractures suggests that there are two main types of diagenetic fluids which are internal runoff karst water and allogenic recharge of lateral freshwater flow.

The dissolution pores formed by Caledonian, Indosinian, and Yanshanian karstifications. Based on the dominant reservoir lithology (dolomite), the fractures generated by multi-stage tectonic movements were coupled with multiphase karstification, forming fracture-related karst reservoirs in the lower Palaeozoic of the southwestern slope of the Bozhong Sag.

Declaration of competing interest

The authors declare that they have no known competing financial interests or personal relationships that could have appeared to influence the work reported in this paper.

Acknowledgement

The authors appreciate the anonymous reviewers for their valuable comments, China National Offshore Oil Corporation (Tianjin Branch) for supporting the exploration data, and Dr. Shi Sun from Chengdu University of technology for his valuable help.

This work was supported by the National Major Science and Technology Project of the Thirteenth Five Year Plan (No. 2016ZX05024-003-010), National Natural Science Foundation of China (No. 42002123), and the Open Fund of State Key Laboratory of Oil and Gas Reservoir Geology and Exploitation (Chengdu Univerisity of Technology, No. PLC2020031).

Appendix A. Supplementary data

Supplementary data to this article can be found online at https://doi.org/10.1016/j.petsci.2023.03.021.

References

Aadnoy, B.S., Bell, J.S., 1998. Classification of drilling-induced fractures and their relationship to in-situ stress directions. Log. Anal. 39 (6), 27–40.

Allen, M.B., Macdonald, D., Xun, Z., et al., 1997. Early Cenozoic two-phase extension and late Cenozoic thermal subsidence and inversion of the Bohai Basin, northern China. Mar. Petrol. Geol. 14 (7), 951–972. https://doi.org/10.1016/S0264-8172(97)00027-5.

Ameen, M.S., Buhidma, I.M., Rahim, Z., 2010. The function of fractures and in-situ stresses in the Khuff reservoir performance, onshore fields, Saudi Arabia. AAPG Bull. 94 (1), 27–60. https://doi.org/10.1306/06160909012.

Aubert, D., Stille, P., Probst, A., Gauthier-Lafaye, F., et al., 2002. Characterization and migration of atmospheric REE in soils and surface waters. Geochem. Cosmochim. Acta 66 (19), 3339–3350. https://doi.org/10.1016/S0016-7037(02)00913-4.

Awdal, A., Healy, D., Alsop, G.I., 2016. Fracture patterns and petrophysical properties of carbonates undergoing regional folding: a case study from Kurdistan, N Iraq. Mar. Petrol. Geol. 71, 149–167. https://doi.org/10.1016/j.marpetgeo.2015.12.017.

Azmy, K., Brand, U., Sylvester, P., Gleeson, S.A., et al., 2011. Biogenic and abiogenic low-Mg calcite (bLMC and aLMC): evaluation of seawater-REE composition, water masses and carbonate diagenesis. Chem. Geol. 280 (1–2), 180–190. https://doi.org/10.1016/j.chemgeo.2010.11.007.

Azmy, K., Lavoie, D., Wang, Z., et al., 2013. Magnesium-isotope and REE compositions of Lower Ordovician carbonates from eastern Laurentia: implications for the origin of dolomites and limestones. Chem. Geol. 356, 64–75. https://doi.org/10.1016/j.chemgeo.2013.07.015.

Badiozamani, K., 1973. The dorag dolomitization model, application to the middle Ordovician of Wisconsin. J. Sediment. Res. 43, 965–984. https://doi.org/10.1306/74D728C9-2B21-11D7- 864000102C1865D.

Baertschi, P., 1976. Absolute 18O content of standard mean ocean water. Earth Planet Sci. Lett. 31 (3), 341–344. https://doi.org/10.1016/0012-821X(76)90115-1.

Barton, C.A., Zoback, M.D., 2002. Discrimination of natural fractures from drilling-

induced wellbore failures in wellbore image data-implications for reservoir permeability. SPE Reservoir Eval. Eng. 5 (3), 249–254. https://doi.org/10.2118/78599-PA.
Bau, M., Dulski, P., 1996. Distribution of yttrium and rare-earth elements in the Penge and Kuruman iron-formations, transvaal Supergroup, South Africa. Precambrian Res. 79 (1–2), 37–55. https://doi.org/10.1016/0301-9268(95)00087-9.
Bosworth, W., Khalil, S., Clare, A., et al., 2014. Integration of Outcrop and Subsurface Data during the Development of a Naturally Fractured Eocene Carbonate Reservoir at the East Ras Budran Concession, Gulf of Suez, Egypt, vol. 374. Geological Society, London, Special Publications, pp. 333–360. https://doi.org/10.1016/S0016-7037(02)00913-4.
Brand, U., Veizer, J., 1980. Chemical diagenesis of a multicomponent carbonate system; 1, Trace elements. J. Sediment. Res. 50 (4), 1219–1236. https://doi.org/10.1306/212F7BB7-2B24-11D7-8648000102C1865D.
Brudy, M., Zoback, M., 1999. Drilling-induced tensile wall-fractures: implications for determination of in-situ stress orientation and magnitude. Int. J. Rock Mech. Min. 36 (2), 191–215. https://doi.org/10.1016/S0148-9062(98)00182-X.
Cai, D.S., 2001. Strike-slip and pull-apart structure study and its significance to petroleum exploration on Laizhouwan sag, Bohai area. Acta Pet. Sin. 22 (2), 19–25. https://doi.org/10.7623/syxb200102004 (in Chinese).
Cao, J., Zhang, Y., Hu, W., et al., 2005. The Permian hybrid petroleum system in the northwest margin of the Junggar Basin, northwest China. Mar. Petrol. Geol. 22 (3), 331–349. https://doi.org/10.1016/j.marpetgeo.2005.01.005.
Cao, Z., Zhang, H., Liu, G., et al., 2015. Main control factors and distribution prediction of high-quality carbonate reservoirs in the Nanpu Sag,Bohai Bay Basin. Oil Gas Geol. 36 (1), 103–110. https://doi.org/10.11743/ogg20150113.
Chen, A., Xu, S., Yang, S., et al., 2018. Ordovician deep dolomite reservoirs in the intracratonic Ordos Basin, China: depositional model and Diagenetic evolution. Energy Explor. Exploit. 36 (4), 850–871. https://doi.org/10.1177/0144598718778171.
Chiarella, D., Longhitano, S.G., Tropeano, M., 2017. Types of mixing and heterogeneities in siliciclastic- carbonate sediments. Mar. Petrol. Geol. 88, 617–627. https://doi.org/10.1016/j.marpetgeo.2017.09.010.
Davies, G.R., Smith Jr., L.B., 2006. Structurally controlled hydrothermal dolomite reservoir facies: an overview. AAPG Bull. 90, 1641–1690. https://10.1306/05220605164.
Deines, Peter, 1980. Chapter 9 - the Isotopic Composition of Reduced Organic Carbon. Elsevier B.V, pp. 329–406.
Derry, L.A., Keto, L.S., Jacobsen, S.B., et al., 1989. Sr isotopic variations in upper Proterozoic carbonates from Svalbard and east Greenland. Geochem. Cosmochim. Acta 53 (9), 2331–2339. https://doi.org/10.1016/0016-7037(89)90355-4.
Elderfield, H., Gieskes, J.M., Baker, P.A., et al., 1982. 87sr/86sr and 18o/16o ratios, interstitial water chemistry and diagenesis in deep-sea carbonate sediments of the ontong java plateau. Geochim. Cosmochim. Acta 46 (11), 2259–2268. https://doi.org/10.1016/0016-7037(82)90199-5.
Friedman, G.M., Sanders, J.E., 1967. Chapter 6 origin and occurrence of Dolostones 1. Dev. Sedimentol. 9, 267–348.
Fu, H., Han, J., Meng, W., et al., 2017. Forming mechanism of the Ordovician karst carbonate reservoirs on the northern slope of central Tarim Basin. Nat. Gas. Ind. 4 (4), 294–304. https://doi.org/10.1016/j.ngib.2017.03.001.
Gromet, L.P., Haskin, L.A., Korotev, R.L., et al., 1984. The "North American shale composite": its compilation, major and trace element characteristics. Geochem. Cosmochim. Acta 48 (12), 2469–2482. https://doi.org/10.1016/0016-7037(84)90298-9.
Hao, Y., Luo, M., Xu, Z., et al., 2014. Division of sedimentary basins and its tectonic evolution in North China from Newproterozoic to Mesozoic. Earth Sci. 39 (8), 1230–1242. https://doi.org/10.3799/dqkx.2014.106.
Hou, G.T., Qian, X.L., Cai, D.S., 2001. The tectonic evolution of Bohai Basin in Mesozoic and Cenozoic time. Acta Sci. Nat. Univ. Pekin. 37 (6), 845–851. https://10.13209/j.0479-8023.2001.143.
Hoefs, J., 1997. Stable Isotope Geochemistry, fourth ed. Springer-Verlag, Berlin.
Hou, M., Cao, H., Li, H., et al., 2019. Characteristics and controlling factors of deep buried-hill reservoirs in the BZ19-6 structural belt, Bohai sea area. Nat. Gas. Ind. 6 (4), 305–316. https://doi.org/10.1016/j.ngib.2019.01.011.
Hou, L., Zhang, C., Lin, Y., et al., 2020. From oblique arc-continent collision to orthogonal plate subduction in the southeastern central Asia Orogenic Belt during palaeozoic: evidence from superimposed folds at the northern margin of the north China Craton. J. Asian Earth Sci. 200, 104499. https://doi.org/10.1016/j.jseaes.2020.104499.
Hsü, K.J., Schneider, J., 1973. Progress Report on Dolomitization — Hydrology of Abu Dhabi Sabkhas, Arabian Gulf, the Persian Gulf. Springer, Berlin, Heidelberg, pp. 409–422. https://doi.org/10.1007/978-3-642-65545-6_20.
Hu, S., O Sullivan, P., Raza, A., et al., 2001. Thermal history and tectonic subsidence of the Bohai Basin, northern China: a Cenozoic rifted and local pull-apart basin. Phys. Earth Planet. In. 126 (3–4), 221–235. https://doi.org/10.1016/S0031-9201(01)00257-6.
Hu, W.X., Chen, Q., Wang, X.L., et al., 2010. REE models for the discrimination of fluids in the formation and evolution of dolomite reservoirs. Oil Gas Geol. 31 (6), 810–818. https://doi.org/10.1016/S1876-3804(11)60008-6 (in Chinese).
Hu, Z.C., Zhang, W., Liu, Y.S., et al., 2015. Wave" signal-smoothing and mercury-removing device for laser ablation quadrupole and multiple collector ICPMS analysis: application to lead isotope analysis. Anal. Chem. 87 (2), 1152–1157. https://doi.org/10.1021/ac503749k.
Huang, S., 1997. A study on carbon and strontium isotopes of late Paleozoic carbonate rocks in the upper Yangtze platform. Acta Geol. Sin. 17 (1387), 32. https://doi.org/10.1093/humrep/17.6.1604.
Huang, B., Zhu, R., Otofuji, et al., 2000. The Early Paleozoic paleogeography of the North China block and the other major blocks of China. Chin. Sci. Bull. 45, 1057–1065. https://doi.org/10.1007/BF02887174.
Huang, S.J., Qing, H.R., Huang, P.P., et al., 2008. Evolution of strontium isotopic composition of seawater from Late Permian to Early Triassic based on study of marine carbonates, Zhongliang Mountain, Chongqing, China. Sci. China Earth Sci. 51, 528–539. https://doi.org/10.1007/s11430-008-0034-3.
Huang, L., Liu, C., Zhou, X., et al., 2012. The important turning points during evolution of Cenozoic basin offshore the Bohai Sea: evidence and regional dynamics analysis. Sci. China Earth Sci. 55, 476–487. https://doi.org/10.1007/s11430-011-4359-y.
Huang, S.J., Huang, K.K., Zhong, Y.J., et al., 2017. Carbon isotope composition and comparison of lower triassic marine carbonate rocks from southern Longmenxia section in Guang'an, Sichuan Basin. China Earth Sci. 60, 80–94. https://doi.org/10.1007/s11430-016-5156-y.
Hudson, J.D., 1977. Stable isotopes and limestone lithification. J. Geol. Soc. (London, U.K.). 133, 637–660. https://doi.org/10.1144/gsjgs.133.6.0637.
Ionov, D., Harmer, R.E., 2002. Trace element distribution in calcite–dolomite carbonatites from Spitskop: inferences for differentiation of carbonatite magmas and the origin of carbonates in mantle xenoliths. Earth Planet Sci. Lett. 198 (3–4), 495–510. https://doi.org/10.1016/S0012-821X(02)00532-0.
Jin, M., Zeng, W., Tan, X., et al., 2014. Characteristics and controlling factors of beach-controlled karst reservoirs in Cambrian Longwangmiao formation, Moxi-Gaoshiti area, Sichuan Basin, NW China. Petrol. Explor. Dev. 41 (6), 712–723. https://doi.org/10.1016/S1876-3804(14)60085-9.
Jing, X., 2016. Carbonate reservoir within the ordovician in the Dongpu area, Bohai Bay Basin, eastern China: diagenesis and diagenetic evolution. In: September 9, 2016 AAPG/SEG International Conference & Exhibition, Cancun, Mexico.
Jones, C.E., Jenkyns, H.C., 2001. Seawater strontium isotopes, oceanic anoxic events, and Seafloor hydrothermal activity in the Jurassic and Cretaceous. Am. J. Sci. 301 (2), 112–149. https://doi.org/10.2475/ajs.301.2.112.
Kaufman, A.J., Jacobsen, S.B., Knoll, A.H., 1993. The Vendian record of Sr and C isotopic variations in seawater: implications for tectonics and paleoclimate. Earth Planet Sci. Lett. 120 (3–4), 409–430. https://doi.org/10.2475/ajs.301.2.112.
Kawabe, I., Toriumi, T., Ohta, A., et al., 1998. Monoisotopic REE abundances in seawater and the origin of seawater tetrad effect. Geochem. J. 32 (4), 213–229. https://doi.org/10.2343/geochemj.32.213.
Keeton, G.I., Pranter, M.J., Cole, R.D., et al., 2015. Stratigraphic architecture of fluvial deposits from borehole images, spectral-gamma-ray response, and outcrop analogs, Piceance Basin, ColoradoStratigraphic Architecture of Fluvial Deposits from Borehole Images. AAPG Bull. 99 (10), 1929–1956. https://doi.org/10.1306/05071514025.
Keith, M.L., Weber, J.N., 1964. Carbon and oxygen isotopic composition of selected limestones and fossils[J]. Geochim. Cosmochim. Acta. 28 (10–11), 1787–1816. https://doi.org/10.1016/0016-7037(64)90022-5.
Khoshbakht, F., Memarian, H., Mohammadnia, M., 2009. Comparison of Asmari, Pabdeh and Gurpi formation's fractures, derived from image log. J. Pet. Sci. Eng. 67 (1–2), 65–74. https://doi.org/10.1016/j.petrol.2009.02.011.
Kovalenko, I., Yarmolyuk, V.V., Kovach, V.P., et al., 2004. Isotope provinces, mechanisms of generation and sources of the continental crust in the Central Asian mobile belt: geological and isotopic evidence. J. Asian Earth Sci. 23 (5), 605–627. https://doi.org/10.1016/S1367-9120(03)00130-5.
Lai, J., Wang, G., Wang, S., et al., 2018. A review on the applications of image logs in structural analysis and sedimentary characterization. Mar. Petrol. Geol. 95, 139–166. https://doi.org/10.1016/j.marpetgeo.2018.04.020.
Li, S.Z., Suo, Y.H., Dai, L.M., et al., 2010. Development of the Bohai Bay Basin and destruction of the North China Craton. CNKI:SUN:DXQY.0.2010-04-009. (in Chinese). Earth Sci. Front. 17 (4), 64.
Li, Y., Qi, L., Zhang, S., et al., 2019. Characteristics and development mode of the Middle and Lower Ordovician fault-karst reservoir in Shunbei area, Tarim basin. Acta Pet. Sin. 40 (12), 1470–1484. https://doi.org/10.7623/syxb201912006.
Liang, J., Wang, H., Bai, Y., et al., 2016. Cenozoic tectonic evolution of the Bohai Bay Basin and its coupling relationship with Pacific Plate subduction. J. Asian Earth Sci. 127, 257–266. https://doi.org/10.1016/j.jseaes.2016.06.012.
Liang, H., Xu, F., Xu, G., et al., 2019. Geochemical characteristics and origins of the diagenetic fluids of the Permian Changxing Formation calcites in the Southeastern Sichuan Basin: evidence from petrography, inclusions and Sr, C and O isotopes. Mar. Petrol. Geol. 103, 564–580. https://doi.org/10.1016/j.marpetgeo.2019.02.015.
Lima, B., Tedeschi, L.R., Pestilho, A., et al., 2020. Deep-burial hydrothermal alteration of the Pre-Salt carbonate reservoirs from northern Campos Basin, offshore Brazil: evidence from petrography, fluid inclusions, Sr, C and O isotopes. Mar. Petrol. Geol. 133, 104143. https://doi.org/10.1016/j.marpetgeo.2019.104143.
Liu, Y.S., Hu, Z.C., Gao, S., et al., 2008. In situ analysis of major and trace elements of anhydrous minerals by LA-ICP-MS without applying an internal standard. Chem. Geol. 257 (1–2), 34–43. https://doi.org/10.1016/j.chemgeo.2008.08.004.
Liu, S.G., Shi, H.X., Wang, G.Z., et al., 2007. formation mechanism of lower Paleozoic carbonate reservoirs in Zhuanghai Buried hill. Nat. Gas. Ind. 27, 1–5. https://doi.org/10.3321/j.issn:1000-0976.2007.10.001 (in Chinese).
Liu, D., Cai, C., Hu, Y., et al., 2021. Multistage dolomitization and formation of ultra-deep lower Cambrian Longwangmiao formation reservoir in central Sichuan Basin, China. Mar. Petrol. Geol. 123, 104752. https://doi.org/10.1016/j.marpetgeo.2020.104752.
Ma, X., Xu, Y., Li, Y., et al., 2009. Research on hydrocarbon enrichment in condensate

gas reservoirs in Qianmiqiao buried hill. Nat. Gas. Ind. 29, 25–26. https://doi.org/10.3787/j.issn.1000-0976.2009.04.006 (in Chinese).
Macrae, N.D., Nesbitt, H.W., Kronberg, B.I., 1992. Development of a positive Eu anomaly during diagenesis. Earth Planet Sci. Lett. 109 (3–4), 585–591. https://doi.org/10.1016/0012-821X(92)90116-D.
Mason, B., 1966. The enstatite chondrites. Geochem. Cosmochim. Acta 30 (1), 23–39. https://doi.org/10.1016/0016-7037(66)90089-5.
Masuda, A., Nakamura, N., Tanaka, T., 1973. Fine structures of mutually normalized rare-earth patterns of chondrites. Geochem. Cosmochim. Acta 37 (2), 239–248. https://doi.org/10.1016/0016-7037(73)90131-2.
Mccrea, J.M., 1950. On the isotopic chemistry of carbonates and a Paleotemperature scale. J. Chem. Phys. 18 (6), 840–857. https://doi.org/10.1063/1.1747785.
Melim, L.A., Scholle, P.A., 2002. Dolomitization of the Capitan Formation forereef facies (Permian, west Texas and New Mexico): seepage reflux revisited. Sedimentology 49 (6), 1207–1227. https://doi.org/10.1046/j.1365-3091.2002.00492.x.
Mogi, K., 1971. Effect of the triaxial stress system on the failure of dolomite and limestone. Tectonophysics 11 (2), 111–127. https://doi.org/10.1016/0040-1951(71)90059-X.
Nie, X., Zou, C., Pan, L., et al., 2013. Fracture analysis and determination of in-situ stress direction from resistivity and acoustic image logs and core data in the Wenchuan Earthquake Fault Scientific Drilling Borehole- 2 (50–1370 m). Tectonophysics 593, 161–171. https://doi.org/10.1016/j.tecto.2013.03.005.
Nothdurft, L.D., Webb, G.E., Kamber, B.S., 2004. Rare earth element geochemistry of Late Devonian reefal carbonates, Canning Basin, Western Australia: confirmation of a seawater REE proxy in ancient limestones. Geochem. Cosmochim. Acta 68 (2), 263–283. https://doi.org/10.1016/S0016-7037(03)00422-8.
Palmer, M.R., Edmond, J.M., 1989. The strontium isotope budget of the modern ocean. Earth Planet Sci. Lett. 92 (1), 11–26. https://doi.org/10.1016/0012-821X(89)90017-4.
Purser, B.H., Brown, A., Aissaoui, D.M., et al., 1994. Nature, origin and evolution of porosity in dolomites. Special Publ. Int. Assoc. Sedimentol. 21, 283–308. https://doi.org/10.1002/9781444304077.ch16.
Qing, H., Mountjoy, E.W., 1994. Formation of coarsely crystalline, hydrothermal dolomite reservoirs in the Presqu'ile barrier, Western Canada sedimentary basin. AAPG Bull. 78 (1), 55–77. https://doi.org/10.1306/BDFF9014-1718-11D7-8645000102C1865D.
Radwan, A.E., Trippetta, F., Kassem, A.A., et al., 2021. Multi-scale characterization of unconventional tight carbonate reservoir: insights from October oil filed, Gulf of Suez rift basin, Egypt. J. Pet. Sci. Eng. 197, 107968. https://doi.org/10.1016/j.petrol.2020.107968.
Reid, S., Dewing, K., Sharp, R., 2013. Structural and diagenetic origin of breccias in the carbonate-hosted Polaris Zn–Pb deposit, Nunavut, Canada. Ore Geol. Rev. 55, 110–124. https://doi.org/10.1016/j.oregeorev.2013.05.003.
Ren, C.Q., Gao, X.Z., Jiang, H., et al., 2018. Characteristics and favorable area prediction of Ordovician buried-hill carbonate reservoirs in the Bozhong 21-2 tectonic belt, Bohai Bay Basin, China. Petrol. Sci. Technol. 36 (17), 1374–1381. https://doi.org/10.1080/10916466.2018.1474222.
Saller, A.H., 1984. Petrologic and geochemical constraints on the origin of subsurface dolomite, Enewetak Atoll: an example of dolomitization by normal seawater. Geology 12 (4), 217–220. https://doi.org/10.1130/0091-7613(1984)122.0.CO;2.
Schwinn, G., Markl, G., 2005. REE systematics in hydrothermal fluorite. Chem. Geol. 216 (3–4), 225–248. https://doi.org/10.1016/j.chemgeo.2004.11.012.
Shao, S., Ye, L., 1999. Geochemical characteristics of carbonate rock weathering and forming soil in the center area of Guizhou Province. CNKI:SUN:JXTW.0.1999-S2-121.(in Chinese). Chin. Sci. Bull. 44, 218–219.
She, M., Shou, J., Shen, A., et al., 2016. Experimental simulation of dissolution law and porosity evolution of carbonate rock. Petrol. Explor. Dev. 43 (4), 616–625. https://doi.org/10.1016/S1876-3804(16)30072-6.
Shields, G., Stille, P., 2001. Diagenetic constraints on the use of cerium anomalies as palaeoseawater redox proxies: an isotopic and REE study of Cambrian phosphorites. Chem. Geol. 175 (1–2), 29–48. https://doi.org/10.1016/S0009-2541(00)00362-4.
Sholkovitz, E., Shen, G.T., 1995. The incorporation of rare earth elements in modern coral. Geochem. Cosmochim. Acta 59 (13), 2749–2756. https://doi.org/10.1016/0016-7037(95)00170-5.
Sholkovitz, E.R., Landing, W.M., Lewis, B.L., 1994. Ocean particle chemistry: the fractionation of rare earth elements between suspended particles and seawater. Geochem. Cosmochim. Acta 58 (6), 1567–1579. https://doi.org/10.1016/0016-7037(94)90559-2.
Spotl, C., Pitman, J.K., 1998. Saddle (Baroque) Dolomite in Carbonates and Sandstones: A Reappraisal of a Burial- Diagenetic Concept, Carbonate Cementation in Sandstones. Distribution Patterns and Geochemical Evolution, pp. 437–460. https://doi.org/10.1002/9781444304893.ch19.
Taylor, H.P., 1974. The application of oxygen and hydrogen isotope studies to Problems of hydrothermal alteration and ore deposition. Econ. Geol. 69 (6), 843–883. https://doi.org/10.2113/gsecongeo.69.6.843.
Taylor, H.P., Sheppard, S.M., 1986. Igneous rocks; I, Processes of isotopic fractionation and isotope systematics. Rev. Mineral. Geochem. 16 (1), 227–271.
Turekian, K.K., Wedepohl, K.H., 1961. Distribution of the elements in some major units of the earth's crust. Geol. Soc. Am. Bull. 72 (2), 175–192. https://doi.org/10.1130/0016-7606(1961)72[175:DOTEIS]2.0.CO.
Veizer, J., Hoefs, J., 1976. The nature of O18/O16 and C13/C12 secular trends in sedimentary carbonate rocks. Geochem. Cosmochim. Acta 40 (11), 1387–1395. https://doi.org/10.1016/0016-7037(76)90129-0.
Wang, D.R., 2000. Stable isotope geochemistry of oil and gas. Pet Ind Press Beijing 164 (171–173), 179–183.
Wang, B., Al-Aasm, I.S., 2002. Karst-controlled diagenesis and reservoir development: example from the Ordovician main-reservoir carbonate rocks on the eastern margin of the Ordos basin, China. AAPG Bull. 86 (9), 1639–1658. https://doi.org/10.1306/61EEDD28-173E-11D7-8645000102C1865D.
Wang, L., Hu, W., Wang, X., et al., 2014. Seawater normalized REE patterns of dolomites in Geshan and Panlongdong sections, China: implications for tracing dolomitization and diagenetic fluids. Mar. Petrol. Geol. 56, 63–73. https://doi.org/10.1016/j.marpetgeo.2014.02.018.
Wang, Z., Lv, X., Li, Y., et al., 2021. Natural fracture opening preservation and reactivation in deep sandstones of the Kuqa foreland thrust belt. Tarim Basin. Mar. Petrol. Geol. 127, 104956. https://doi.org/10.1016/j.marpetgeo.2021.104956.
Weeks, A.W., 1967. Geology of Petroleum, Geology of Petroleum. W.H. Freeman and Company. https://doi.org/10.1306/SP812.
Wierzbicki, R., Dravis, J.J., Al-Aasm, I., et al., 2006. Burial dolomitization and dissolution of upper Jurassic Abenaki platform carbonates, deep Panuke reservoir, Nova Scotia, Canada. AAPG Bull. 90 (11), 1843–1861. https://doi.org/10.1306/03200605074.
Xiang, P., Ji, H., Shi, Y., Huang, Y., Sun, Y., Xu, X., Zou, S., 2020. Petrographic, rare earth elements and isotope constraints on the dolomite origin of Ordovician Majiagou Formation (Jizhong Depression, North China). Miner. Resour. Res. 117, 104374. https://doi.org/10.1016/j.marpetgeo.2020.104374.
Xiong, Y., Tan, X., Zuo, Z., et al., 2019. Middle Ordovician multi-stage penecontemporaneous karstification in North China: implications for reservoir genesis and sea level fluctuations. J. Asian Earth Sci. 183, 103969. https://doi.org/10.1016/j.jseaes.2019.103969.
Xiong, Y., Tan, X., Zhong, S., et al., 2022. Dynamic paleokarst geochemistry within 130 Myr in the middle ordovician Shanganning carbonate platform, North China. Palaeogeogr. Palaeocl. 591, 110879. https://doi.org/10.1016/j.palaeo.2022.110879.
Yan, Z.B., Guo, F.S., Pan, J.Y., et al., 2005. Application of C, O and Sr isotope composition of carbonates in the research of paleoclimate and paleooceanic environment. Contrib. Geol. Miner. Resour. Res. 20 (1), 53–56. https://doi.org/10.6053/j.issn.1001-1412.2005.1.010 (in Chinese).
Yang, X., Mei, Q., Wang, X., et al., 2018. Indication of rare earth element characteristics to dolomite petrogenesis- A case study of the fifth member of Ordovician Majiagou Formation in the Ordos Basin, central China. Mar. Petrol. Geol. 92, 1028–1040. https://doi.org/10.1016/j.marpetgeo.2017.12.004.
Ye, T., Wei, A., Sun, Z., et al., 2019. The reservoir characteristics and their significance for deliverability in metamorphic granite buried hill: a case study from the JZS oil field in the Liaodong Bay Basin, NE China. Arabian J. Geosci. 12, 630. https://doi.org/10.1007/s12517-019-4823-0.
Ye, T., Chen, A., Niu, C., et al., 2020a. Characteristics and vertical zonation of large: cale granitic reservoirs, a case study from Penglai oil field in the Bohai Bay Basin, North China. Geol. J. 55 (12), 8109–8121. https://doi.org/10.1002/gj.3932.
Ye, T., Wei, A., Gao, K., et al., 2020b. New sequence division method of shallow platform with natural gamma spectrometry data: implication for reservoir distribution—a case study from Majiagou Formation of Bozhong 21–22 structure, Bohai Bay Basin. Carbonates Evaporites 35, 116. https://doi.org/10.1007/s13146-020-00654-w.
Ye, T., Chen, A., Niu, C., et al., 2022. Effective fractures linked with tectonic reactivation and multiple genetic fluids in the ultradeep Paleozoic carbonate buried hills of the Bozhong sag, North China. Mar. Petrol. Geol. 140, 105642. https://doi.org/10.1016/j.marpetgeo.2022.105642.
Ying, W., Wang, Y., Zhao, X., et al., 2005. Oil and gas reservoir formation characteristics of fault-block buried hills in Jiyang Depression. Nat. Gas. Ind. 25 (2), 10–13.
Yu, F., Qi, J., Wang, C., 2002. Tectonic deformation of Indosinian period in eastern part of north China. J. China Inst. Min. Technol. 31 (4). https://doi.org/10.3321/j.issn:1000-1964.2002.04.017 (in Chinese).
Yurimoto, H., Duke, E.F., Papike, J.J., et al., 1990. Are discontinuous chondrite-normalized REE patterns in pegmatitic granite systems the results of monazite fractionation? Geochem. Cosmochim. Acta 54 (7), 2141–2145. https://doi.org/10.1016/0016-7037(90)90277-R.
Zhai, M., Santosh, M., Zhang, L., 2011. Precambrian geology and tectonic evolution of the North China Craton. Gondwana Res. 20 (1), 1–5. https://doi.org/10.1016/j.gr.2011.04.004.
Zhang, S., Zhao, Y., Davis, G.A., et al., 2014. Temporal and spatial variations of Mesozoic magmatism and deformation in the North China Craton: implications for lithospheric thinning and decratonization. Earth Sci. Rev. 131, 49–87. https://doi.org/10.1016/j.earscirev.2013.12.004.
Zhang, W., Zhou, Q., Yang, W., et al., 2021. Research on thin layer structure identification and sedimentary facies of middle and deep layers Based on reflection Coefficient inversion—By taking Dongying formation of CFD oilfield in Bohai offshore as an example. Open J. Geol. 11 (6), 197–209. https://doi.org/10.4236/ojg.2021.116012.
Zheng, J., Dai, H., 2018. Subduction and retreating of the western Pacific plate resulted in lithospheric mantle replacement and coupled basin-mountain respond in the North China Craton. Sci. China Earth Sci. 61, 406–424. https://doi.org/10.1007/s11430-017-9166-8.
Zheng, Y.F., Zhang, S.B., Zhao, Z.F., et al., 2007. Contrasting zircon Hf and O isotopes in the two episodes of Neoproterozoic granitoids in South China: implications for growth and reworking of continental crust. Lithos 96 (1–2), 127–150. https://doi.org/10.1016/j.lithos.2006.10.003.

Zhu, L., Wang, Z., Feng, Q., et al., 2020. Genesis of dolomite in the upper assemblage of the Ordovician Majiagou Formation in the southeastern Sulige gas field, Ordos Basin, China: evidence from C, O, and Sr isotopes and major and trace elements. Energy Explor. Exploit. 38 (6), 2729–2751. https://doi.org/10.1177/0144598720948195.

Zong, K., Klemd, R., Yuan, Y., et al., 2017. The assembly of Rodinia: the correlation of early Neoproterozoic (ca. 900 Ma) high-grade metamorphism and continental arc formation in the southern Beishan Orogen, southern Central Asian Orogenic Belt (CAOB). Precambrian Res. 290, 32–48. https://doi.org/10.1016/j.precamres.2016.12.010.